JGR Atmospheres

RESEARCH ARTICLE
10.1029/2022JD037138

Special Section:
Advances in scaling and modeling of land-atmosphere interactions

Space-Scale Resolved Surface Fluxes Across a Heterogeneous, Mid-Latitude Forested Landscape

Sreenath Paleri[1], Ankur R. Desai[1], Stefan Metzger[1,2], David Durden[2], Brian J. Butterworth[3,4], Matthias Mauder[5,6], Katrin Kohnert[7,8], and Andrei Serafimovich[7,9]

[1]Department of Atmospheric and Oceanic Sciences, University of Wisconsin-Madison, Madison, WI, USA, [2]Battelle, National Ecological Observatory Network, Boulder, CO, USA, [3]Cooperative Institute for Research in Environmental Sciences, University of Colorado, Boulder, CO, USA, [4]NOAA Physical Sciences Laboratory, Boulder, CO, USA, [5]Institute of Hydrology and Meteorology, Technische Universität Dresden, Dresden, Germany, [6]Institute of Meteorology and Climate Research – Atmospheric Environmental Research, Karlsruhe Institute of Technology, Garmisch-Partenkirchen, Germany, [7]GFZ German Research Centre for Geosciences, Potsdam, Germany, [8]Now at German Council of Experts on Climate Change, Berlin, Germany, [9]Now at Deutscher Wetterdienst, Offenbach, Germany

Abstract The Earth's surface is heterogeneous at multiple scales owing to spatial variability in various properties. The atmospheric responses to these heterogeneities through fluxes of energy, water, carbon, and other scalars are scale-dependent and nonlinear. Although these exchanges can be measured using the eddy covariance technique, widely used tower-based measurement approaches suffer from spectral losses in lower frequencies when using typical averaging times. However, spatially resolved measurements such as airborne eddy covariance measurements can detect such larger scale (meso-β, meso-γ) transport. To evaluate the prevalence and magnitude of these flux contributions, we applied wavelet analysis to airborne flux measurements over a heterogeneous mid-latitude forested landscape, interspersed with open water bodies and wetlands. The measurements were made during the Chequamegon Heterogeneous Ecosystem Energy-balance Study Enabled by a High-density Extensive Array of Detectors intensive field campaign. We ask, how do spatial scales of surface-atmosphere fluxes vary over heterogeneous surfaces across the day and across seasons? Measured fluxes were separated into smaller-scale turbulent and larger-scale mesoscale contributions. We found significant mesoscale contributions to sensible and latent heat fluxes through summer to autumn which would not be resolved in single-point tower measurements through traditional time-domain half-hourly Reynolds decomposition. We report scale-resolved flux transitions associated with seasonal and diurnal changes of the heterogeneous study domain. This study adds to our understanding of surface-atmospheric interactions over unstructured heterogeneities and can help inform multi-scale model-data integration of weather and climate models at a sub-grid scale.

Plain Language Summary Accurate and reliable knowledge of the surface-atmospheric transport of mass and energy is essential to inform our theories and models of Earth system processes. Conventionally, such transport has been measured by tower-mounted weather instruments that make high-frequency measurements. However, experimental and simulation studies over the last couple of decades have shown that there is an imbalance between incoming, available energy and outgoing transport as observed from tower-mounted setups. A dominant hypothesis addressing this imbalance issue postulates that there exists significant larger landscape scale transport (of the order of 10–100 km) over the course of a day. Single-point tower measurements would not be able to include such transports in their conventional process flows. We use airborne data collected over a mid-latitude temperate forest in Northern-Wisconsin, USA to quantify large-scale transport over the forested domain. Observations were made over the course of single days in July, August, and September to include seasonal landscape transitions. The measured surface-atmospheric exchange is resolved into smaller and larger scale contributions using a space-frequency analysis framework that has been in use for aircraft measured atmospheric data. We report substantial large-scale contributions with daily, seasonal and spatial characteristics.

Key Points:

- Substantial, persistent mesoscale surface-atmospheric fluxes were measured across a heterogeneous mid-latitude forested domain
- Measured fluxes show distinct seasonal and diurnal variations
- Measured mesoscale fractions of sensible and latent heat fluxes do not behave similarly

Supporting Information:

Supporting Information may be found in the online version of this article.

Correspondence to:

S. Paleri,
paleri@wisc.edu

Citation:

Paleri, S., Desai, A. R., Metzger, S., Durden, D., Butterworth, B. J., Mauder, M., et al. (2022). Space-scale resolved surface fluxes across a heterogeneous, mid-latitude forested landscape. *Journal of Geophysical Research: Atmospheres*, *127*, e2022JD037138. https://doi.org/10.1029/2022JD037138

Received 18 MAY 2022
Accepted 16 NOV 2022

1. Introduction

Surface-atmospheric fluxes of energy, momentum, water, carbon, and other scalars are integral components of Earth system processes. Terrestrial ecosystems act as important intermediaries for these exchange processes, influencing Earth's weather and climate systems (Pielke et al., 1998). However, the land-surface is heterogeneous

at multiple scales owing to spatial variability in multiple properties and the atmospheric responses to these heterogeneous surface forcings through the fluxes of energy, water, carbon, and other scalars are also scale-dependent and nonlinear (Avissar & Schmidt, 1998). Since the scales of transport vary from Kolmogorov microscale in the turbulent regime to the mesoscale it is not easy to resolve the contributions from all of the relevant scales directly using observations or simulations (Bou-Zeid et al., 2020).

The primary transport process in the atmospheric boundary layer (ABL) is turbulence and the surface-atmospheric turbulent fluxes can be directly measured using the eddy-covariance (EC) technique (Aubinet et al., 2012; Foken, 2017). The EC technique uses Reynolds decomposition of the Navier-Stokes equation for momentum and scalar transport, with the assumptions of stationarity and horizontal homogeneity, to calculate turbulent fluxes in the ABL. Tower based EC measurements are widely used to study ecosystem level biosphere-atmosphere interactions and quantify surface-atmospheric fluxes (Aubinet et al., 1999; Baldocchi et al., 2001). Even with careful experimental design and quality control, they are however limited by their surface flux footprints (i.e., part of the upstream surface contributing to the measured flux). Moreover, requirements for stationarity can complicate sampling flux contributions from lower frequencies as well (Desjardins et al., 1997; Mahrt, 2010).

So, a good first order sanity check on tower measured turbulent fluxes would be to check for the closure of the measured surface energy budget, evaluating whether available energy (the difference between measured net radiation and ground heat flux) within the control volume sampled by the tower is balanced by the measured sum of turbulent sensible and latent heat fluxes (Foken, 2008; Foken et al., 2010; Mauder et al., 2020; Oncley et al., 2007). Such a check would also be important to validate land-surface and biological model parameters such as surface flux parameterizations in weather and climate models, water vapor surface conductances in ecosystem and land-surface models, or validating model predictions of net ecosystem exchanges. However, a persistent surface energy balance residual has been reported in prior investigations across multiple sites in multiple ecosystems (Foken et al., 2010; Mauder et al., 2020; Oncley et al., 2007).

Simulations and observational studies have shown that there can be larger-scale transport linked to landscape variability. Based on their analysis of tower measured EC data Bernhofer (1992) had attributed the residuals to large-scale non-turbulent transport driven by surface gradients. Finnigan et al. (2003) pointed out that the conventionally used averaging windows of 30 min could act as a high pass filter for the data. They also noted that pre-treating tower measured turbulent data by rotating the measurement coordinates so that x-axis of measurement is aligned with the mean horizontal wind could also contribute to the same. Such data processing would remove contributions of motions with periods longer than the averaging times to the covariance being measured. Early Large Eddy Simulation (LES) studies (Inagaki et al., 2006; Kanda et al., 2004; Steinfeld et al., 2007) with idealized surface forcings indicated that transport due to turbulent organized structures and thermally induced mesoscale structures can cause systematic underestimation of fixed point tower flux measurements. Maronga and Raasch (2013) conducted a LES study using measured sensible and latent heat fluxes as imposed surface boundary conditions over the LITFASS-2003 field experiment domain and diagnosed signals of heterogeneity-induced vertical velocities linked to landscape heterogeneities. Using a wavelet analysis of airborne turbulent data during the BOREAS field experiment, Mauder, Desjardins, and MacPherson (2008) quantified the mesoscale transport across a temperate heterogeneous landscape to be 10% of surface measured available energy and of the same order of magnitude as tower measured residuals over the domain. The LES study by K. Xu et al. (2020) employed simulated towers over idealized heterogeneities. Following a spatio-temporal eddy covariance approach for simulated towers they could account for 95% of the available energy with one tower per 40 km^2. Such a spatial approach seems to account for the landscape scale low-frequency transport. The recent LES study by Margairaz et al. (2020) over idealized heterogeneities also shows that fluxes by secondary circulations can account for 5%–10% of near-surface sensible heat fluxes.

These investigations indicate that when surface heterogeneity starts influencing the surface-atmospheric transport, there can be quasi-stationary circulations modulated by the heterogeneity amplitudes and background wind. Such structures could lead to increased advective transport and flux divergences, thereby altering the net transport associated with the turbulent covariance term, measured through the eddy covariance method (Mahrt, 2010; Mauder et al., 2020). Quantifying and diagnosing such a 3-dimensional transport and horizontal variability of surface atmospheric fluxes over heterogeneous domains in the field calls for the deployment of intensive instrumentation that can sample the surface atmospheric exchanges at multiple, overlapping scales (Wulfmeyer et al., 2018). Identification and measurement of such structures and their contributions from field observations call for spatially

resolving measurement techniques, such as a distributed tower network (Engelmann & Bernhofer, 2016; Mauder, Desjardins, Pattey, Gao, & van Haarlem, 2008; Morrison et al., 2021; Oncley et al., 2007), airborne measurements (Bange et al., 2002, 2006; Mahrt, 1998; Mauder, Oncley, et al., 2007; Strunin & Hiyama, 2004), scintillometers (Foken et al., 2010; Meijninger et al., 2006; F. Xu et al., 2017) and LiDAR measurements (Drobinski et al., 1998; Eder et al., 2015; Higgins et al., 2013) etc. Spectral analysis of tower measured turbulence data can also give some insight into the nature of flux contributions from the lower frequencies (Gao et al., 2020; G. Zhang et al., 2014; Y. Zhang et al., 2010; Zhou et al., 2019).

Among these measurements, airborne EC measurements are one of the few that can directly measure the spatial distribution of 3D turbulence across a study domain (Mahrt, 1998, 2010). Moreover, with spatial transects, airborne measurements can directly sample contributions from larger (of the order of meso-β 20–200 km, meso-γ 2–20 km, from Orlanski, 1975) scale persistent structures excited by surface heterogeneities. In contrast, for ground-based measurements these larger-scale structures would have to drift by their field-of-view. Airborne transects through a study domain can also pass through multiple quasi-stationary eddies, giving robust statistics for the measured fluxes.

Here, we use airborne turbulence data collected over a heterogeneous mid-latitude forested landscape interspersed with creeks and lakes in the Chequamegon-Nicolet National forest near Park Falls, Wisconsin USA. Through this analysis we aim to address the following research questions:

1. Can spatially resolved airborne eddy covariance identify spatial scales of surface-atmosphere fluxes over heterogeneous surfaces?
2. How do spatial scales of surface-atmospheric fluxes vary across the day and across seasons? What is the role of ABL stability and land-surface variability in modulating these exchanges?
3. What are the ensuing implications for improving the surface energy balance closure or understanding scales of turbulent transport?

The airborne measurements were collected as part of the Chequamegon Heterogeneous Ecosystem Energy-balance Study Enabled by a High-density Extensive Array of Detectors (CHEESEHEAD19) field experiment (Butterworth et al., 2021), conducted from July–October 2019. The experimental study design aimed to sample the landscape transition from late summer to early fall and the associated ABL responses. The CHEESEHEAD19 airborne data set presents a unique opportunity to analyze long periods of airborne EC over long legs (30 km) in a heterogeneous region over multiple times a year with differing patterns of surface sensible and latent heat fluxes. The data set provides an extensive set of scenarios to investigate our research questions and derive principles from. To quantify and spatially localize contributions from all the relevant scales of transport we calculate the surface atmospheric fluxes through the wavelet cross-scalograms of the turbulent data (Mauder, Desjardins, & MacPherson, 2007; Metzger et al., 2013; Strunin & Hiyama, 2004, 2005). A wavelet based analysis can distinguish surface-atmosphere fluxes at multiple scales and quantify the contributions from larger scales, allowing us to resolve scale transport across space.

To those ends, we pose the following null and alternative hypotheses:

- H0: Mesoscale transport is an invariant, small fixed fraction of the total flux.
- HA: Persistent contributions of larger scale (in the range of meso-β to meso-γ) fluxes to the daytime sensible and latent heat fluxes exist with diurnal and seasonal variations.

2. Data and Methods

2.1. Experiment Description

The Chequamegon Heterogeneous Ecosystem Energy-balance Study Enabled by a High-density Extensive Array of Detectors (CHEESEHEAD19) was a field campaign conducted from June to October 2019, in Chequamegon-Nicolet National Forest, Wisconsin, USA. The experiment was designed to intensively sample and scale land-surface properties and the ABL responses to it across a heterogeneous mid-latitude forested landscape interspersed with creeks and lakes. The two main motivations for the field experiments were to determine how spatial heterogeneity of the surface impacts the local energy balance and atmospheric circulations and to evaluate how the presence or absence of these circulations influence the representativeness of single-point surface fluxes compared to the grid average.

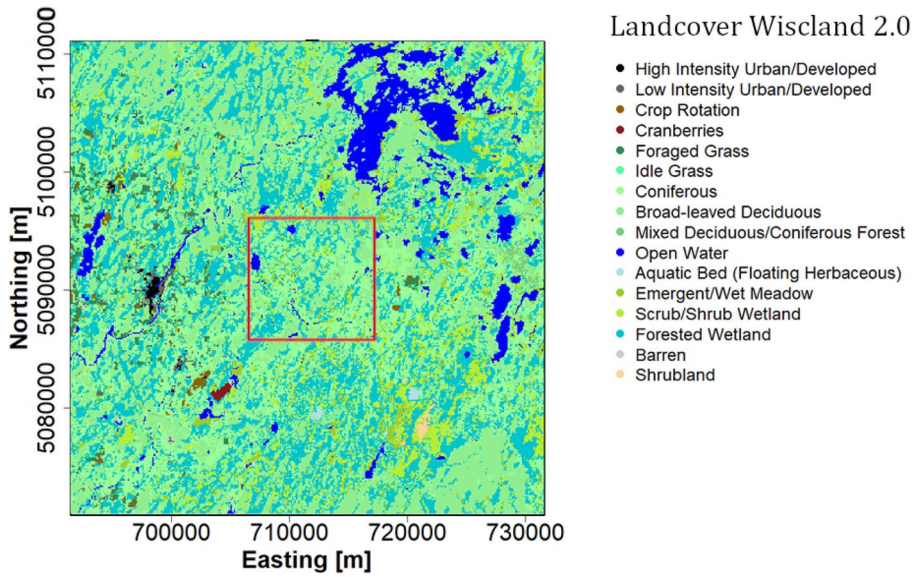

Figure 1. Land cover classes for a 40 × 40 km area bounding the study domain from the Wiscland 2.0 land cover classification data set. The 10 × 10 km core CHEESEHEAD19 domain is shown in the red box.

Measurements were made using a suite of observing platforms over a core 10 × 10 km domain (that would fit within a "grid cell" of a weather/climate model) and a 30 × 30 km extended domain centered on the Department of Energy AmeriFlux regional tall tower (US PFa 45.9459°N, −90.2723°W). EC fluxes have been measured nearly continuously at the US PFa tall tower since 1996 (Berger et al., 2001) and the study domain is well documented in previous studies that used flux data from the tall tower (Davis et al., 2003; Desai, 2014; Desai et al., 2015). The field campaign collected measurements of ground-based and airborne fluxes, atmospheric profiles, and surface environment at varying scales. Butterworth et al. (2021) give a detailed overview of the field experiment design and all of the deployed instrumentation.

Figure 1 shows the land cover classes across the extended domain from the State of Wisconsin Department of Natural Resources Land Cover Data (Wiscland 2.0) accessed from https://dnr.wisconsin.gov/maps/WISCLAND. The vegetation and land cover within the study domain is characteristic of a mid-latitude temperate forest, dominated by conifers, broadleaf deciduous trees, and wetlands. The study domain is also interspersed with open water bodies, the largest being the Flambeau Lake to the North-Eastern sector of the domain. The presence of such a vertically and horizontally heterogeneous surface, with maximum canopy heights ranging from a couple of meters to 35 m, gives a unique opportunity to study surface atmospheric exchanges over unstructured land-surface heterogeneity where multiple surface properties and roughness elements vary at multiple scales, addressing a crucial gap in our current understanding (Bou-Zeid et al., 2020). Site descriptions of 17 flux tower sites, set up as part of the National Center for Atmospheric Research (NCAR)-Integrated Surface Flux Station (ISFS) network, within the core 10 × 10 km domain can be found at http://cheesehead19.org. This gives an idea about the variation in surface and vegetation properties across the domain. The extended 3-month duration of the field experiment also allows us to sample the shift in the surface energy budget partitioning as the study domain shifts from a latent heat-dominated late summer landscape to a more sensible heat flux-dominated early autumn landscape.

2.2. Airborne Intensive Observations

Airborne turbulence data were collected over the extended domain with the University of Wyoming King Air (UWKA) research aircraft. The UWKA is a Beechcraft King Air 200T model, a part of the National Science Foundation's Lower Atmosphere Observation Facility that has been in use for in situ airborne measurements of cloud and boundary layer properties since 1977 (A. Rodi, 2011; Wang et al., 2012). Three 7-day Intensive Observation Periods (referred to as IOPs henceforth) were conducted during the experiment during each month from July to September when all the available field instrumentation were deployed simultaneously. During these IOPs, the UWKA Research Aircraft flew linear transects across the domain on 4 days sampling turbulent measurements

Table 1
Dates, Times, Flight Patterns of the Flights Analyzed for All Three Intensive Observation Periods (IOPs)

Date	Domain start time (UTC)	Domain end time (UTC)	Flight number	Flight pattern	Wind dir (deg)	Wind speed (m/s)	Short Wave incoming (W/m^2)
2019-07-09	14:00	16:00	RF01	West-East 2	180	6	643
2019-07-09	19:00	21:00	RF02	West-East 2	210	5	701
2019-07-11	14:00	16:00	RF03	West-East 1	345	3	852
2019-07-11	19:00	21:00	RF04	West-East 1	45	5	829
2019-07-12	14:00	16:00	RF05	West-East 2	225	6	686
2019-07-12	18:00	21:00	RF06	West-East 2	225	5	642
2019-07-13	14:00	16:00	RF07	South-East 2	330	3	833
2019-07-13	19:00	21:00	RF08	South-West 1	330	3	869
2019-08-20	14:00	16:00	RF09	South-East 1	215	3	244
2019-08-20	19:30	22:00	RF10	South-East 1	180	1	648
2019-08-21	14:00	16:30	RF11	South-West 1	0	5	663
2019-08-21	19:00	21:30	RF12	South-West 1	315	6	639
2019-08-23	14:00	16:30	RF15	West-East 2	80	0.5	681
2019-08-23	19:30	21:30	RF16	West-East 2	120	3	703
2019-09-24	14:00	16:30	RF17	South-East 1	230	4	503
2019-09-24	19:00	21:30	RF18	South-East 1	180	5	342
2019-09-25	14:40	17:00	RF19	South-West 1	270	5	573
2019-09-25	19:30	22:00	RF20	South-West 1	310	5	326
2019-09-26	14:00	16:30	RF21	South-East 1	270	3	518
2019-09-26	18:45	21:15	RF22	South-East 1	265	5	422
2019-09-28	14:30	17:00	RF23	West-East 1	353	3	674
2019-09-28	19:00	21:30	RF24	West-East 1	15	3	500

of wind velocities, temperature, water vapor, and CO_2, at a frequency of 25 Hz (Table 1). The airborne experiment was designed with the help of numerical experiments to maximize spatial coverage over the domain, ensure adequate sampling of larger scale eddies and ensure crew safety. Metzger et al. (2021) provide details about the numerical simulations, analysis framework, and design strategy used to come up with the final flight patterns for the airborne measurements. Figure 2 shows these different patterns and their respective waypoints. Each research flight pattern was composed of flight transects connecting consecutive waypoints. We refer to these individual transects as flight legs. The flight legs were designed to be 30 km so that they extend about 10 km outside of the core 10 × 10 km domain to ensure that enough mesoscale contributions to the core 10 × 10 km domain could be sampled.

On each day there was a morning (14:00–17:00 Universal Time Coordinated) flight and an afternoon (19:00–22:00 Universal Time Coordinated) research flight. Each research flight (RF) performed 30 km down-and-back transects at 100 and 400 m above ground between two consecutive waypoints, alternating between straight and diagonal passes. The first leg of all transects was at 400 m and the return legs at 100 m. For example, from Table 1, on 11 July 2019, the morning research flight was RF03 with the WE1 (west-east 1) flight pattern. For RF03, from Figure 2, the first leg was from waypoint 1 to waypoint 2 at 400 m and the second leg was back to 1 from 2 at 100 m. Then the third leg would be from 1 to 4, diagonally at 400 m and so on.

The primary scientific purpose of the higher 400 m legs was to observe the temperature and moisture profiles using a downward pointing Compact Raman Lidar. The low-altitude legs were flown at 100 m since this was the lowest altitude deemed safe to fly for the maximum forest canopy height of 35 m. This also ensures that the measurements taken were in the surface layer and above the roughness sublayer of the forested domain. Wavelet cross-scalograms of the atmospheric turbulence data from the 100 m legs were used to calculate the surface atmospheric fluxes during the IOPs.

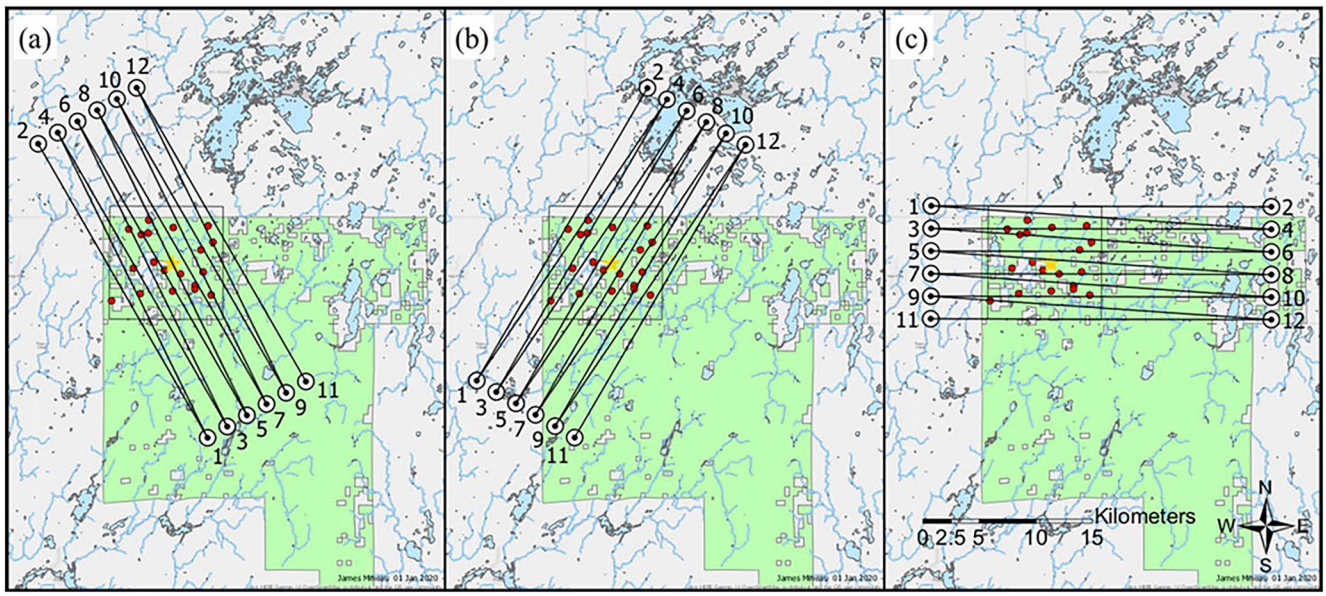

Figure 2. Three sets of waypoints define three distinct flight patterns, named after the starting location and direction of their first waypoint: (a) south-east (SE), (b) south-west (SW), and (c) west-east (WE). Flying the numbered waypoints either in ascending order (SE1, SW1, WE1) or descending order (SE2, SW2, WE2) results in six distinct flight sequences that maximize data coverage under different wind conditions. Map credit: James Mineau, University of Wisconsin-Madison (Metzger et al., 2021: Figure 14, published by Atmospheric Measurement Techniques, reproduced with permissions under https://creativecommons.org/licenses/by/4.0/).

2.3. Wavelet Analysis

Wavelet transforms can reveal information localized in both space and frequency domains (Farge, 1992; Mahrt et al., 1998) for a given input signal. This distinct property makes wavelet based time-frequency analysis suited for the analysis of in-homogeneous or non-stationary geophysics data, unlike other conventional methods such as a Fourier transform or its windowed version (Kumar and Foufoula-Georgiou 1994) that require periodicity. Airborne measurements over the CHEESEHEAD19 study domain sampled a spatially and temporally varying surface flux field, including measurements over varying surface roughness heights, canopy heights, and soil properties. In this regard, a wavelet decomposition of the airborne turbulence measurements over the heterogeneous domain can extract scale-resolved information and quantify contributions from larger-scale quasi-stationary modes induced by landscape scale heterogeneities. A wavelet analysis also yields a space-scale mapping of the measured fluxes, throughout the day and across seasons.

The wavelet functions and analysis methods were developed for time-frequency analysis (Farge, 1992; Thomas & Foken, 2005), but since we are working with spatial data, we have expanded upon the existing methodology to facilitate space-scale analysis. In wavelet analysis, one starts with choosing a wavelet function or mother wavelet, Ψ, which is localized in both space and frequency domains and has zero mean (Farge, 1992; Torrence & Compo, 1998). The mother wavelet of choice for this study is the complex Morlet wavelet, $\Psi(\eta) = \pi^{-1/4} e^{i\omega_0 \eta} e^{-\eta^2/2}$, with the frequency parameter $\omega_0 = 6$ as suggested by Torrence and Compo (1998). The Morlet wavelet is a complex sine wave modulated by a Gaussian envelope and has been in use for the analysis of atmospheric turbulence data because the resulting wavelet transform offers good localization in the scale domain (Mauder, Desjardins, & MacPherson, 2007; Strunin et al., 2004; Thomas & Foken, 2005). The mother wavelet Ψ can be stretched and squeezed or translated across the spatial domain to construct "daughter wavelets' $\Psi_{p,a,b}$ where a is the dilation parameter and b is the translation parameter.

$$\Psi_{p,a,b}(x) = \frac{1}{a^p} \Psi\left(\frac{x-b}{a}\right) = \Psi_p(\eta) \tag{1}$$

Here, p is a normalization parameter and is set as 1/2 for this study, and η is a non-dimensional coordinate in the space-scale domain. The wavelet transform is a convolution, $\int f(x)\Psi^*_{p,a,b}\, dx$, of a given signal $f(x)$ with the daughter wavelets to yield a series of wavelet coefficients $T(a, b)$ that are functions of the dilation and translation parameters. $\Psi^*_{p,a,b}$ is the complex conjugate of $\Psi_{p,a,b}$. Since both the scale and the location of the mother wavelet

filter kernels can be adjusted, such an analysis can yield localized details matched to their scale (subject to the fundamental Heisenberg uncertainties, Addison, 2017). In the discrete limit, for a spatial series $f(n)$ with N data points, the wavelet coefficients become,

$$T_f(a,b) = \sum_{n=0}^{N} f(n)\Psi^*_{p,a,b} \tag{2}$$

Different localizations or "daughter wavelets" of the same mother wavelets are scaled and translated across the input data to extract information about the amplitudes and locations of matching details corresponding to equivalent amplitudes at corresponding locations present in the input signal. This allows us to calculate the wavelet spectral energy density (E_f) for a chosen dilation and locations from the coefficients as $E_f(a, b) = |T_f(a, b)|^2$, referred to as the wavelet scalogram matrix. Consequently, the variance (σ_f) of the chosen signal, $f(x)$ can be calculated by averaging the matrix and summing across the scales,

$$\sigma_f = \frac{\delta j \delta t}{C_\delta N} \sum_{j=0}^{J} \sum_{n=0}^{N-1} \frac{|T_f(a_j, b_n)|^2}{a_j} \tag{3}$$

Here, $\delta t = 0.04$ for the 25 Hz data and δj, the discrete intervals in scale, is set as 0.125, setting up 8 octaves, following Torrence and Compo (1998). C_δ is an admissibility constant defined for each mother wavelet of choice, to reconstruct the original series from its wavelet transform. For the complex Morlet wavelet $C_\delta = 0.776$ (Torrence & Compo, 1998). Similarly, given two signals, $f(n)$ and $g(n)$, a cross-scalogram matrix can be calculated as $T_f(a,b) \times T_g^*(a,b)$, where * denotes a complex conjugate. Their co-variance can be estimated by integrating their co-spectral energy spanning the constituent scales across their cross-scalograms as:

$$cov_{ab} = \frac{\delta j \delta t}{C_\delta N} \sum_{j=0}^{J} \sum_{n=0}^{N-1} \frac{T_f(a_j, b_n)\, T_g^*(a_j, b_n)}{a_j} \tag{4}$$

A sample wavelet cross-scalogram of vertical wind and water vapor mole fraction space series is shown in Figure 3b. Integrating the cross-scalogram in scale and converting the variance magnitudes to energy units lets us calculate the associated scale-integrated flux space series, shown in Figure 3a. The shading in the cross-scalograms denote the amplitude of the wavelet coefficients. The peaks in the calculated latent heat flux space series can be seen coinciding with segments of strong amplitudes, which vary throughout the length of the series reflecting the variability of surface atmospheric transport across the transect.

The summation operation in Equation 4 can be performed over any desired subset of scales to calculate the wavelet covariance between two chosen signals (Mauder, Desjardins, & MacPherson, 2007; Torrence & Compo, 1998). Doing so gives the contribution from those ranges of scales to the total covariance. This presents the opportunity to quantify the contributions from different scales over choice of spatial segments by integrating across subsets of scales without neglecting contributions from scales larger than the choice of spatial segment. For this study, we chose a flux partitioning scale of 2 km to distinguish between small-scale boundary layer turbulence and larger mesoscale contributions following Mauder, Desjardins, and MacPherson (2007) and Strunin et al. (2004). The 2 km cutoff serves as proxy for the maximum boundary layer height, which would be the largest scale for the turbulent energy producing eddies in the ABL. ABL height shifts are observed in response to temporal factors such as seasonal and diurnal cycles (Figure 7) as well as spatial variations in land-cover heterogeneity. However, the 2 km threshold seems to be a good indicator for the relative variation in the magnitude of mesoscale fluxes (Section 3.1).

2.4. Flux Measurement and Data Processing

Wavelet based flux processing of the campaign data was done using the eddy4R family of open-source packages (Metzger et al., 2017). The 25 Hz airborne data product used in this study was preprocessed by the UWKA research crew to include routine UWKA corrections and is hosted at the NCAR-Earth Observing Laboratory (EOL) repository as part of the public CHEESEHEAD19 project data repository (French et al., 2021). Table 2 gives details of the UWKA instrumentation used for measuring aircraft and atmospheric state variables. Each research aircraft deployment had a resulting 25 Hz NetCDF data file. The data from these files with all the

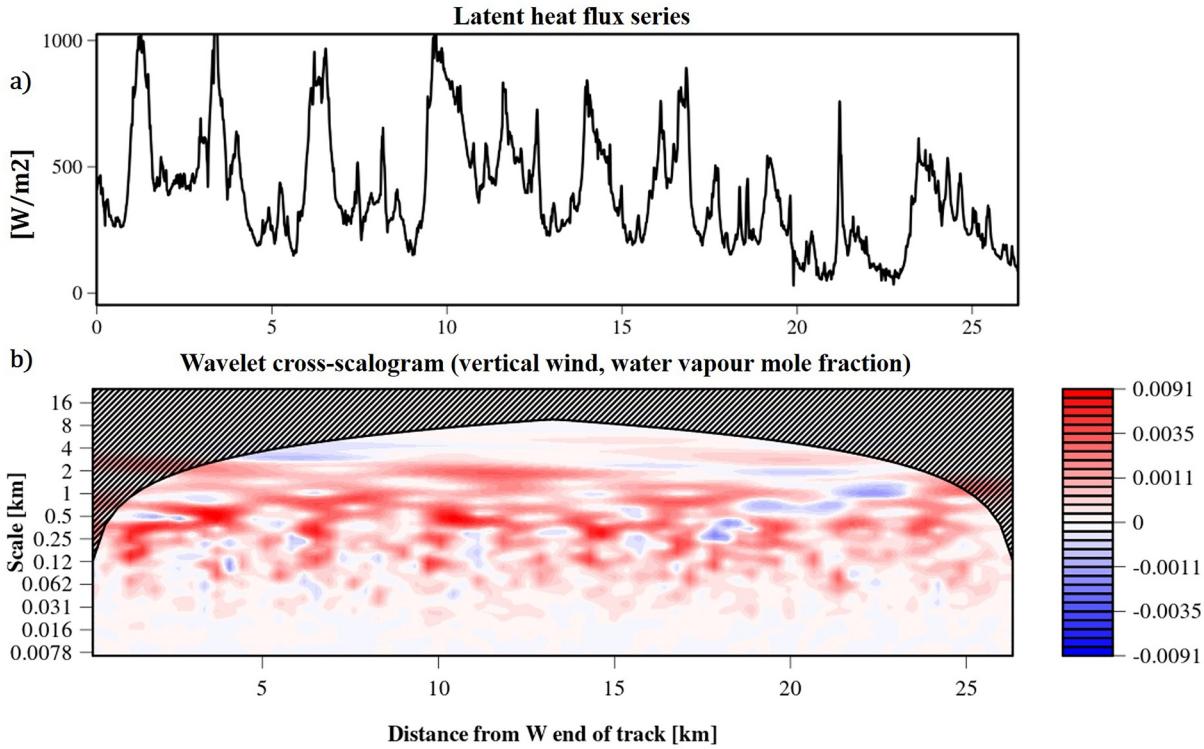

Figure 3. A sample wavelet cross-scalogram (b) between vertical velocity and water vapor mole fraction illustrating the scale-resolved spatial contributions along RF02 flight leg 04. This cross-scalogram is calculated by integrating across spatial scales along the *y*-axis giving the latent heat flux space series shown in (a). The shading in (b) denotes amplitudes with red shaded regions denoting positive contributions, while blue shades denote negative and white neutral. Hashed portions represent the cone of influence for edge effects.

Table 2
Univerity of Wyoming King Air Instrumentation Details

Measurement	Instrument	Description
Aircraft state		
3D position, ground velocity, orientation, body-axis longitudinal/lateral/vertical acceleration	Applanix AV 410 GPS/Inertial Measurement Unit	Applanix Position Orientation System for Airborne Vehicles; combined solid-state/GPS system with real-time differential corrections; higher accuracy post processed data available (Haimov & Rodi, 2013)
Altitude	Stewart Warner APN159 radar altimeter	Altitude above ground level Range:0–60,000 ft (18,288 m); accuracy 1%; resolution: 0.24 ft (0.07 m)
Airspeed	Honeywell Laseref SM Inertial Reference System (IRS)	Range:0–4,095 kts; accuracy: 13.5 ft/s; resolution: 0.0039 kts
Flow angles	Rosemount 858AJ five-hole gust probe	Range:±15; accuracy:0.2; resolution:0.00015
Atmospheric state		
Air temperature	Reverse-flow housing with Minco platinum-resistive element (A. R. Rodi & Spyers-Duran, 1972)	Range: −50 C to +50 C; accuracy: 0.5 C; resolution: 0.006°C
Wind components	Applanix AV 410 GPS/Inertial Measurement Unit	Earth relative 3D wind
Atmospheric pressure	Rosemount 1501 HADS	High accuracy digital sensing module static pressure, corrected for dynamic effects (A. R. Rodi & Leon, 2012); Range: 0–1,034 mb; accuracy: 0.5 mb, resolution: 0.006 mb
Water vapor	LICOR Li-7500A	LI-COR LI-7500 open-path CO_2/H_2O gas analyzer

necessary atmospheric and aircraft state variables were read in to the eddy4R processing environment. The air temperature, pressure, and water vapor mole fraction data were lag corrected by maximizing the cross-correlation with vertical velocity data (Hartmann et al., 2018). Flight leg start and end times were used to slice the research flight data into flight leg specific data. This ensured that only data collected during the linear transects across the study domain are used for the study and data collected during the over turnings at the way-point edges are excluded. Convective boundary layer (CBL) height was measured during the IOP days by two Radiometrics MP-3000A Microwave Radiometers (MWRs) deployed roughly 45 km west and south to the WLEF tall tower (locations in Figure 1a, Duncan et al., 2022 and data available from Adler et al., 2021) at the Lakeland and Prentice airports in Wisconsin. CBL heights from the hourly averaged data product were also added to the flight leg level data.

Flux calculations were performed individually for each flight leg. The missing data threshold was set to 90%. Each flight leg covered spatial transects of 25–30 km, depending on whether they were horizontal or diagonal along the cardinal wind directions (Section 2.2). With 25 Hz frequency and an averaged airspeed of 86 m/s, the mean spatial resolution of the data was 3.5 m. Hence, the average number of data points for the flight leg level data sets analyzed for each flight was 8,200, with data sets ranging from 6,500 to 9,000 data points. The minimum daughter wavelet frequency was set at the Nyquist frequency of 12.5 Hz and the maximum depended on the duration of the data set (averaging to 30 km). The wavelet frequencies were converted to scale space using the Fourier wavelength for the Morlet wavelet (Torrence & Compo, 1998). Adaptive, high-frequency corrections were applied to the wavelet scalograms following (Nordbo & Katul, 2013). A spatial series of wavelet covariance fluxes was calculated from the wavelet cross-scalograms using Equation 4, for overlapping subintervals of 1,000 m (Metzger et al., 2013). The 1,000 m subintervals were centered above each cell of the 100 m resolution Wiscland 2.0 land cover classification data set for the study domain (Figure 1, Section 2.5), giving window averaged flux measurements every 100 m. Random and systematic flux errors were calculated following Lenschow et al. (1994) and Lenschow and Stankov (1986). The turbulent scale flux space series was calculated by setting the maximum wavelet scale for scalograms at 2 km. The mesoscale flux contributions were then calculated as the difference between fluxes from all scales and the turbulent scale fluxes. While creating summary statistics and figures an absolute threshold of 10 Wm^{-2} was applied for sensible and latent heat fluxes to ensure that the fluxes are well resolved. A hard threshold of (−400, 1,000) Wm^{-2} was set for the LE space series and (−50,400) Wm^{-2} for the H series to remove spurious measurements.

2.5. Footprint Modeling and Flux Topographies

Footprint of a flux measurement refers to the effective finite measurement area upwind of the sensors from where the eddies are being sampled from Foken et al. (2006). Kljun et al. (2004) are a 1D parameterization of a backward Lagrangian model (Kljun et al., 2002) in the stable to strongly convective ABL. Since this is not crosswind-integrated, Metzger et al. (2013) combined it with a Gaussian crosswind dispersion function. This is implemented in the analysis currently. The model requirements measurements of friction velocity (u^*), measurement height (z), standard deviation of the vertical wind (σ_w), and the aerodynamic roughness length (z_0). With the exception of z_0 all the other variables are directly measured by the UWKA. z_0 is inferred from a logarithmic wind profile with the integrated universal function for momentum exchange after Businger et al. (1971) in the form of Högström (1988) (Metzger et al., 2013). For each of the 1,000 m subintervals geolocated above the centers of the land cover classification data set an individual footprint weight matrix was calculated as the subintervals were moved forward in space along the flight leg. This generated a footprint weight matrix for every flight leg analyzed (Figure 4a). This matrix is used to weigh and cumulatively sum the land cover contributions along the flight leg to give the space series of land-surface contribution to the flux series (Figures 4b and 4c). Latent heat flux space series presented in Figure 4c is the same series whose cross-scalogram was presented in Figure 3b.

To investigate how the flux contributions vary over the course of a research flight and spatially over the domain, the measured fluxes are back-projected to their surface source as gridded two-dimensional data following the flux topography method of Mauder, Desjardins, and MacPherson (2008). Flux topographies are the footprint-weighted flux contributions measured across the domain from the airborne data (Amiro, 1998). The flux topographies are calculated over a 10 × 10 km CHEESEHEAD19 domain sub-set at the 100 m resolution of the flux space series. The calculated fluxes are projected back to the surface grid, weighted at each grid cell by the cumulative flux footprint from all the sub-intervals in a processed flight leg.

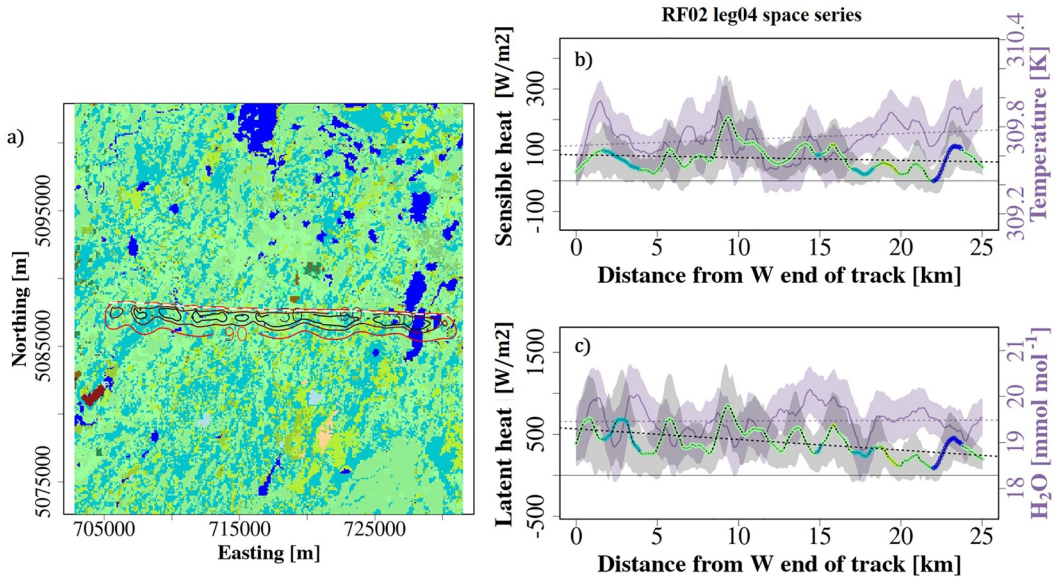

Figure 4. Footprint weights and window averaged flux space series calculated for RF02 flight leg 04. (a) Cumulative flux footprint along the flight leg (shown in white dashed lines). Contour lines show 30%, 60%, and 90% source area contributions to the fluxes measured. (b) Space series of measured air temperature (purple line) and calculated sensible heat flux (black line with colored dots). Shading around each line indicate the random sampling errors. Color of the circles in the flux series indicate the dominating land cover type. Legend in Figure 1. (c) Space series of measured water vapor mole fraction (purple line) and calculated latent heat flux (black line with colored dots). Colored and shaded the same as (b). Two hundred fifty one flux estimates were calculated at each 100 m grid cells located below the flight leg as seen in (a). Giving a 1,000 m window averaged version of Figure 3a.

For each flight leg from an RF, a flux topography was calculated, then the cumulative footprint weighted contribution (F_{ij}) for an RF was calculated at each grid cell in space (Kohnert et al., 2017) according to Equation 5.

$$F_{ij} = \frac{\sum_j^N \left(\sum_i^M f_{i,j} * g_{i,j} \right)}{\sum_j^N \left(\sum_i^M g_{i,j} \right)} \quad (5)$$

In Equation 5, f denotes the flux magnitudes measured, g the footprint weights, with the number of flight legs going from j to N and indices i to M denoting the number of footprint weights. For example, for RF02 leg 04, the calculated flux space series (Figures 4b and 4c) were projected on to the flux footprint source area shown in Figure 4a, weighed in space by the footprint weights. Source areas with low footprint values (<0.05%) are excluded from the analysis. This procedure was repeated for all the flight legs of RF02 using Equation 5 to calculate the cumulative, footprint weighted spatial distribution of the measured fluxes.

3. Results

We start by looking into the scale composition of the fluxes measured across the domain in Section 3.1. To illustrate the seasonal variation and evolution of measured turbulent and mesoscale fluxes we present the seasonally averaged and scale-separated contributions across the IOPs in Section 3.2. Following this, we present the domain-averaged and scale-separated diel data of the fluxes for each of the IOPs. Then the flight averages for all of the research flights analyzed here are also presented. In Section 3.3, we discuss the observed relationship between mesoscale transport and local ABL stability. Then, we investigate the composition of land cover contributions within the footprint of flight legs and how those might relate to the observed mesoscale transport in Section 3.4.

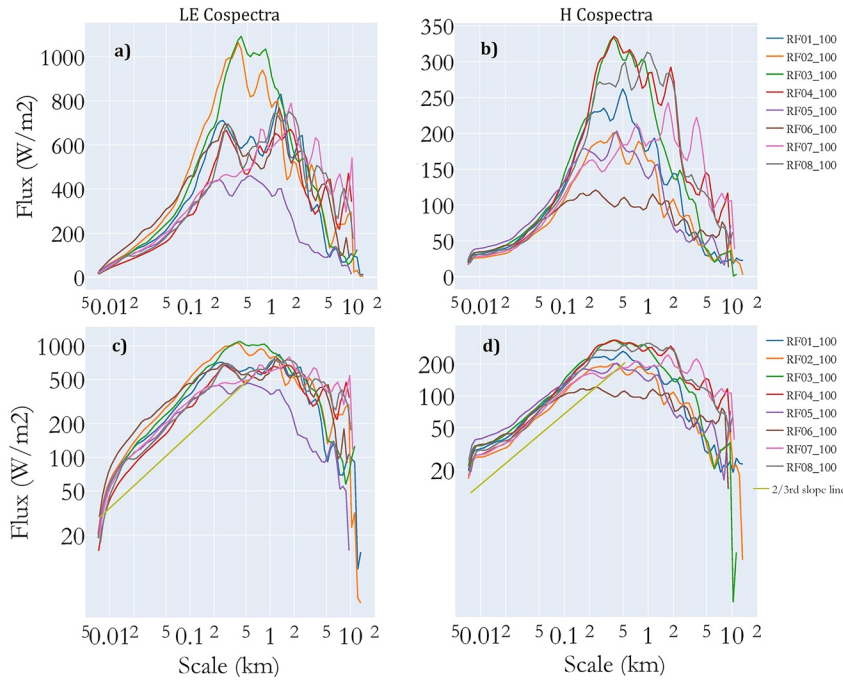

Figure 5. Wavelet cospectra for latent (a, c) and sensible heat (b, d) fluxes measured during each research flight at 100 m above ground during the July Intensive Observation Period (IOP). Cospectra were calculated for each flight leg during the research flights and then ensemble averaged over all the flight legs used in the analysis. The first row, shows a semi-log depiction and the second row shows a log-log representation. Different colors indicate different research flights and the 2/3 slope line. Please note that even though both the subplots in a row (a, b and c, d) share the *y*-axis labels, their ordinate ranges are kept different to better illustrate the variations in sensible heat flux spectra.

3.1. Scale-Resolved Fluxes

Wavelet cospectra for the sensible and latent heat fluxes were calculated for all research flights analyzed (Figures 5 and 6) to investigate the scale-resolved contributions to surface fluxes across the domain. The wavelet cross-scalograms from each flight leg were averaged across the space domain. These were then ensemble averaged across all flight legs that make up a research flight. The cospectra are not normalized to retain the relative magnitudes of the sensible and latent heat fluxes as well as to illustrate the flux magnitudes measured during the different flight campaign days. The flux cospectra follow a 2/3 rd power law scaling in the small scales, indicating the inertial subrange of atmospheric turbulence (Kaimal & Finnigan, 1994). The cospectral power drops suddenly after about 7 m, which is reasonable considering the spatial resolution of the UWKA high-frequency data is 3–4 m, with the average flight speed of 86 m/s and data resolution of 25 Hz. Both semi-log and log-log depictions are included to illustrate the spatial scales spanning the inertial subrange and turbulence production ranges as well as cospectral magnitudes and spectral power variability in the larger scales.

The latent heat flux cospectra calculated for research flights in the July IOP (Figures 5a and 5c) reveal a clustering of secondary maxima between 1 and 2 km. The inertial subrange for most of the flights ends around 200 m, which would allow these peaks to be in the production scales for turbulence or signals of larger-scale non-turbulent structures. The secondary maxima are less prominent in RF02 and RF03 LE cospectra, both with larger magnitude for the measured turbulent fluxes. Their peak is around a spatial scale of 800 m. The peak flux magnitude for the IOP is also from these two flights and is of the order of 1,000 Wm^{-2}. However, the sensible heat flux cospectra for the July IOP does not reveal any such clustering. The cospectra in their log-log representation flatten out into the production scales of turbulence around 200 m for most of the flights (Figure 5d). The magnitudes are also more variable between different flight days, with the peaks in the turbulence production scales reaching out to 300 Wm^{-2}. H cospectral power reduces for the spatial scales larger than 2 km while the LE copsctra still has power in the larger scales.

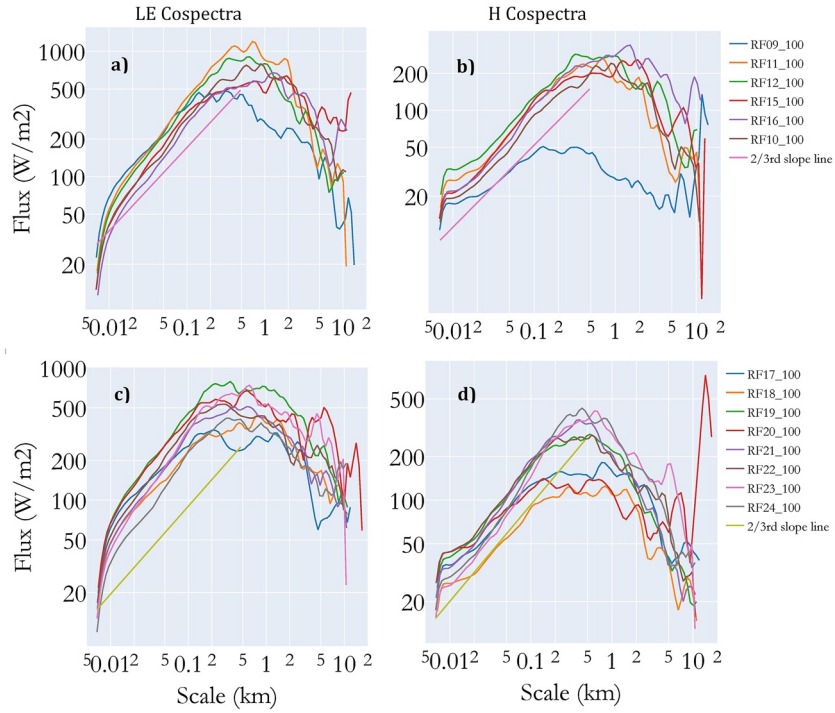

Figure 6. Wavelet cospectra for latent (a, c) and sensible heat (b, d) fluxes measured during each research flight at 100 m above ground during the August (a, b) and September (c, d) Intensive Observation Period (IOP). The first row show cospectra for the August IOP flights and the second row show cospectra for the September IOP flights. Cospectra were calculated for each flight leg during the research flights and then ensemble averaged over all the flight legs used in the analysis. Different colors indicate different research flights and the 2/3 slope line. Please note that even though both the subplots in a row (a, b and c, d) share the *y*-axis labels, their ordinate ranges are kept different to better illustrate the variations in sensible heat flux spectra.

The prominent clustering of secondary peaks is no longer present in the latent heat flux cospectra for the August IOP research flights (Figure 6a). Cospectra for RF 15 and RF 16 show maximum flux magnitudes around spatial scales of 2,000 and 1,200 m respectively (Figures 6a and 6b). Research flights 10, 11, and 12 have LE local maxima around spatial scale of 500 m to 1 km. These three flights measured peak latent heat flux magnitudes of the order of 1,000 Wm^{-2} while the other flights have their maxima around 600 Wm^{-2}. For the LE cospectra, spectral power in the large-scales are similar order of magnitude as the July IOP measured values. The sensible heat flux cospectra for August IOP (Figure 6b) are similar to the July IOP cospectra. They are broader in the turbulence production scales than the latent heat flux cospectra (Figure 6a), with spatial scales ranging from 300 m to 2 km. RF09 has stands out with a low measured H cospectral power due to a rain event during early morning. Apart from this research flight, the other flights measured peak fluxes in the 200–300 Wm^{-2} range.

Most of the sensible heat flux cospectra for research flights in the September IOP show a shorter range of spatial scales in the turbulence production scales (Figure 6d). Research flights 17 and 18 stand out with a broader range of spatial scales in the turbulence production range. The peak cospectral power for sensible heat fluxes are also higher in the September IOP, with values reaching around 400 Wm^{-2}. Compared to the July and August sensible heat flux cospectra, the September cospectral data show lesser power in the larger scales. The latent heat flux cospectral peaks are smaller than the values in the other two IOPs and more variable between different flight days. LE cospectra for RF 19 has a maximum around 800 Wm^{-2} while RF 17 has a double maxima, both around 300 Wm^{-2}. Such a prominent double peak nature is only seen in the RF17 LE cospectra, with the first maxima around 200 m spatial scale and the second one at 1,200 m. A more diffused double peak structure is seen in the cospectra for RF 19, where the peaks are of the same order of magnitude, at around 400 m and 1 km.

The heat flux cospectra do not show a distinct separation of the energy producing turbulent scales and mesoscales of atmospheric motion. The ABL height provides a theoretical maximum for the largest scales of atmospheric turbulence. ABL height was measured during the IOP days by two Radiometrics MP-3000A MWRs deployed

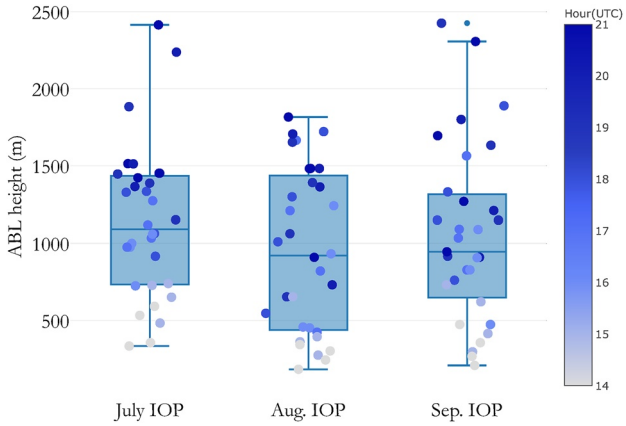

Figure 7. Distribution of hourly Microwave Radiometer measured atmospheric boundary layer (ABL) height during the Intensive Observation Periods (IOPs; data from Adler et al., 2021), colored by the time of day.

roughly 45 km west and south to the AmeriFlux tall tower (locations in Figure 1a, Duncan et al., 2022 and data available from Adler et al., 2021) at the Lakeland and Prentice airports in Wisconsin. Duncan et al. (2022) give an overview of the instruments and presents a validation of the ABL height data with radiosonde measurements during the field experiment. Figure 7 presents the distribution of the hourly averaged boundary layer height measurements, averaged over both the instruments and colored by the time of day. Little change is observed in the median ABL height measured across the IOPs. The boundary layer height increase with the development of the CBL can also be seen. During the July IOP, save for three data points, most values are bound between 300 and 1,500 m. The range of values broaden for the next two IOPs. For the August IOP, the boundary layer height measurements range from 200 to 1,800 m and for the September IOP they range from 200 to 2,000 m. These measurements indicate that 2 km is a reasonable order of magnitude threshold for the large-scale structure/transport across the IOPs and can help partition the contributions from the largest scales of boundary layer turbulence and mesoscale structures.

3.2. Seasonal and Diurnal Variations

IOP averaged flux magnitudes reflect the seasonal shift in the landscape (Figure 8). IOPs were conducted from late summer in the start of July to early autumn at the end of September 2019. In July, the study domain is latent heat flux-dominated and toward the end of September as senescence starts to set in, it transitions to a sensible heat flux-dominated landscape. The mean sensible heat flux magnitude for all scales does not change substantially between the three IOPs and remains around 89 Wm^{-2}. However, there is a substantial variation in the magnitudes of the latent heat fluxes measured across the months. The measured total LE is higher than the total H in the July and August IOPs, increasing from 179 ± 5 to 256 ± 3 Wm^{-2} and then reduces to 69 ± 3 Wm^{-2} in the September IOP (Figure 8 and Table S1 in Supporting Information S1), falling below the total sensible heat flux measured (89 ± 1 Wm^{-2}). The percentage mesoscale and turbulent contributions to the total measured fluxes also show a seasonal variation for the sensible and latent heat fluxes. For the sensible heat flux, the percentage turbulent contribution for the July IOP is 81%, which reduces to a further 77% in August and then increases to 86% in September. Similarly, for latent heat fluxes, the percentage turbulent contribution for the July IOP is the least, at 68%, increasing to 82% in August and then decreasing to 72% for September. When a particular heat flux dominated the surface atmospheric exchange it also had the lowest percentage mesoscale contribution among the IOPs. In August, when the total (turbulent + mesoscale) latent heat flux magnitude is at its maximum at 256 ± 3

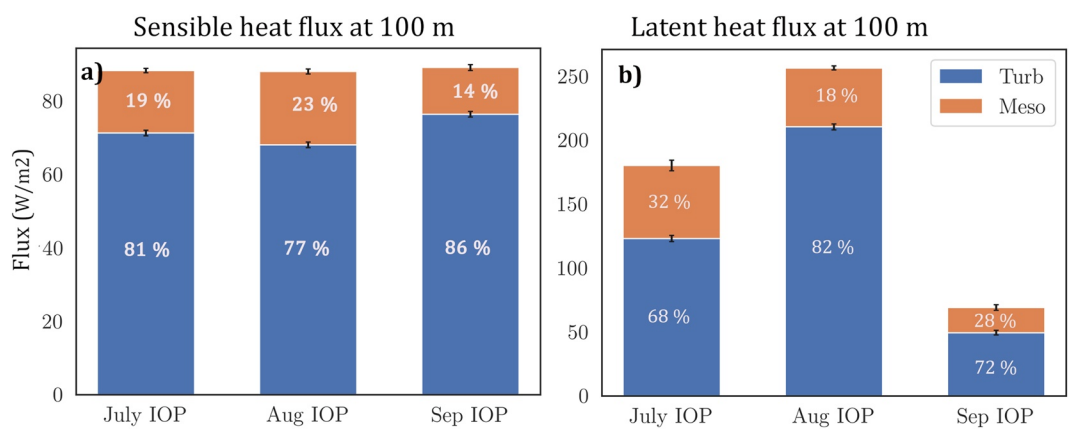

Figure 8. Mean turbulent (blue) and mesoscale (orange) (a) H and (b) LE fluxes for the three Intensive Observation Periods (IOPs) showing seasonal flux transitions. The flux percentages of the total are shown in white within the bars. Please note that even though both the subplots share the *y*-axis label, their ordinate ranges are kept different to better illustrate the variations in sensible heat flux magnitudes.

Wm^{-2}, the mesoscale fraction of the same is at its minimum, at 18%. Similarly, when the evaporative fraction is at its minimum September at 0.76, the sensible heat mesoscale fraction is also at a minimum at 14%.

The sensible heat flux data averaged across the domain and all flight days shows a diurnal cycle for all of the IOPs (Figure 9 column 1, black lines). The calculated turbulent scale fluxes follow the same patterns closely, but mesoscale fluxes do not. For the July IOP data, the total sensible heat flux peaks at 128.8 ± 1.31 Wm^{-2} around 16:20 UTC. In August the sensible heat flux maximum is of the same order, at 121.1 ± 1.3 Wm^{-2} but shifted to later in the afternoon around 20:20 UTC (Figure 9c). The measured fluxes in the August IOP also show sustained values of the order of 100 Wm^{-2} from late morning to after noon (15:50–20:30 UTC) until later in the day toward the end of the afternoon. The September IOP sensible heat flux data has a more pronounced peak at 148.7 ± 1.5 Wm^{-2}. Our scale analysis reveals that this clear diurnal signal is present only for the turbulent scale fluxes which follow the total fluxes diel pattern closely for most of the flight day. In the July IOP the calculated mesoscale sensible heat fluxes peak around 30.8 ± 0.8 Wm^{-2} before noon and in the afternoon there are sustained values around 20 Wm^{-2} till later in the evening toward the end of the research flights. This can also be seen reflected in the difference between the total and turbulent flux diel plots in Figure 9a. Similarly for the August IOP, mesoscale fluxes show sustained values in the afternoon around 25 Wm^{-2}, peaking at 34.8 ± 1 Wm^{-2}. Sensible heat mesoscale values are the lowest in the September IOP as observed earlier in the IOP averaged data. The median value for the IOP data is 11 Wm^{-2}, and the maximum value observed was 18 ± 0.7 Wm^{-2} around 19:30 UTC.

The latent heat fluxes do not show such a clear diurnal variation for the domain averaged data. The domain averaged flux magnitudes are of the same order of magnitudes as the IOP averaged values presented earlier.

The total fluxes measured for all research flights analyzed is presented in Figure 10. This picture at a research flight level reflects the seasonal variation detailed in Figure 8. Flux measurements from RF 2 (9 July afternoon) and RF 3 (11 July morning) stand out in the July IOP data (9–13 July) with total fluxes measured at 430.2 and 436.5 Wm^{-2}. This is due to increased contributions from turbulent latent heat fluxes for the two flights (Figure S2 in Supporting Information S1). The mesoscale contributions measured were of the same order of magnitude as other days of the IOP. Similarly, RF 23 (28 September morning) stands out in the September IOP (24–28 September) with measured turbulent fluxes the same order of magnitude as the late summer IOPs. This was due to an increase in the measured turbulent latent heat fluxes (Figure S6 in Supporting Information S1) due to a rain event earlier that day.

3.3. ABL and Land-Surface Drivers of Transport

3.3.1. ABL Dynamics

The Obukhov length (Monin & Obukhov, 1954; Obukhov, 1946) was calculated for each of the 1,000 m flux calculation windows (Section 2.4) as $L = -u^{*3}\overline{\theta_{v0}}/kgQ_{v0}$. Here, u^* is the measured surface friction velocity (turbulent velocity scale representative of surface shear stress); $g/\overline{\theta_{v0}}$, a buoyancy parameter where g is the gravitational acceleration and $\overline{\theta_{v0}}$ the average surface virtual potential temperature; k is the von Kármán constant set as 0.4 and Q_{v0} the calculated surface kinematic vertical heat flux $\left(\overline{w'\theta'_v}\right)$ of the virtual potential temperature θ_v. The values used for u^*, $\overline{\theta_{v0}}$ and Q_{v0} were the local averages calculated over the 1,000 m spatial subintervals. Since L has units of length, a non-dimensional turbulent surface layer stability parameter $\zeta = \frac{z}{L}$, where z is the measurement height, can be defined (Stull, 1988). Negative values of ζ close to 0 indicate a statically neutral surface layer and as the value decreases, the surface layer becomes more statically unstable.

ζ values were calculated like so for all the flight legs analyzed giving 250–300 values per space series for every leg. The median values were calculated for every flight leg as representative of the spatial transect over the heterogeneous domain. Normalized histograms of median ζ values show that the August IOP is more convective than the other two IOPs with more data points within the $\zeta < -1$ range (Figure 11). On the other hand, the September IOP looks strongly shear driven, with most of the data falling within $\zeta \in [-1, 0]$. In this regard, the July and September IOPs seem to be dynamically similar.

To understand how scale-separated contributions vary with ABL dynamics, we compare the probability density functions (PDFs) of mesoscale flux fractions between shear driven ($\zeta \in [-1, 1]$) and convectively driven

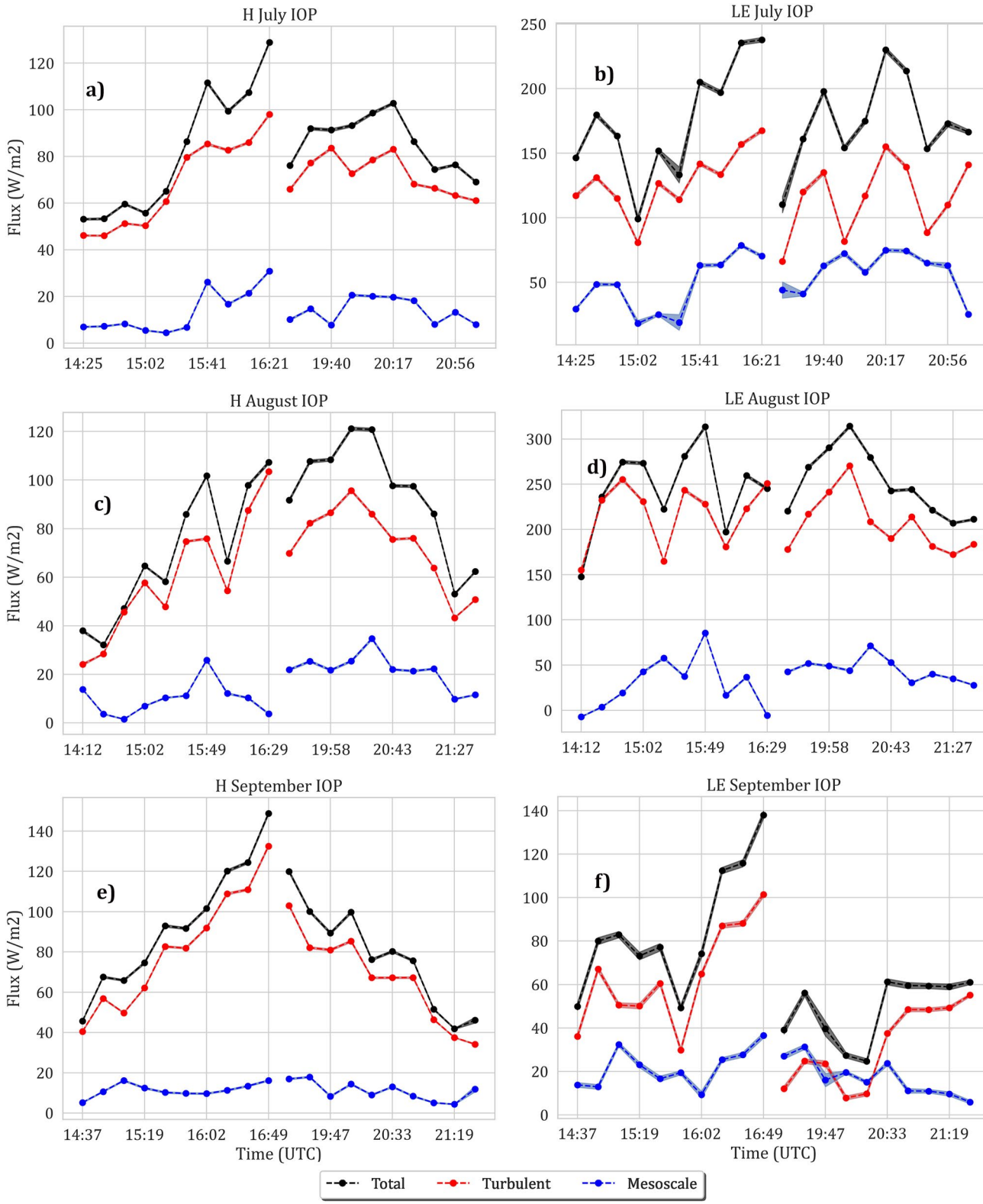

Figure 9.

($\zeta \in [-20, 1]$) ABLs. The mesoscale fractions of the total flux contributions are calculated for each of the 1,000 m subintervals for sensible and latent heat flux space series. Based on the calculated ζ values of their subinterval, the mesoscale flux fraction data were grouped into neutral and unstable categories for all three IOPs. For all six subsets, outlier removal was done for the mesoscale percentage values based on median absolute deviations (Iglewicz & Hoaglin, 1993). Using data from all the subintervals gives us a good number of data points for robust statistical analysis. For N_s denoting the number of data points for neutral, shear driven ABL and N_c denoting the number of data points for unstable, free convectively driven ABL, the July IOP data had $N_s = 15{,}428$ and $N_c = 2{,}203$. Likewise, for the August IOP $N_s = 9{,}298$ and $N_c = 5{,}158$, and for the September IOP $N_s = 17{,}041$ and $N_c = 1{,}308$.

Kernel density estimations (KDEs) are used to calculate PDFs from the airborne spatial data. KDEs are a way to estimate the continuous, non-parametric PDF of a given distribution of random variable using smoothing window functions or kernels (Scott, 1979, 2015). A histogram of the data can provide a non-parametric estimate of the underlying probability density when the bin counts are normalized by the total sample size and multiplied by the bin width. This conventional discrete PDF representation of the data in a histogram uses stacked rectangular bars. In KDEs, a window function (such as a Gaussian kernel with a chosen bandwidth) is employed instead of rectangular bars to estimate a continuous PDF of the data.

In this study, we use Gaussian kernels with a sample size depended band width, given by a rule-of-thumb bandwidth estimate $h = N^{-1/(1+d)}$, where N is the number of data points and d the number of dimensions (1 for the univariate distributions here) following Scott (2015). PDFs were calculated using KDEs for the mesoscale flux fraction distributions in the neutral and unstable regimes. For the sensible heat flux distributions, the two distributions were found to be significantly different from each other for all 3 IOPs using the Mann-Whitney U rank test with 95% confidence. The PDFs show statistically significant higher fraction of mesoscale transport observed in convectively driven ABLs across all the three IOPs (Figure 12).

For latent heat fluxes, the kernel density estimates of mesoscale fraction distributions for the July and August IOPs show higher mesoscale fluxes for convective cases (Figure 13). Performing a Mann-Whitney U rank test again showed that the distributions are significantly different for the two stability regimes at 95% confidence. However, for September IOP the mesoscale transport does not have a preference between a shear or convectively driven ABL. Even though July and September IOPs have similar ABL stability distributions their latent heat mesoscale transport does not show the same behavior, hinting at the role of seasonality through changing surface characteristics and insolation.

The PDFs of sensible and latent heat mesoscale fractions show values when the flux fractions are >1 and <0 (albeit near-zero for the sensible heat distributions when mesoscale fractions are >1). These occur when the measured mesoscale and turbulent fluxes are out of phase with each other. For both sensible and latent heat fluxes, the histograms of turbulent and mesoscale fluxes when the mesoscale fraction is greater than 1 show higher, positive values of mesoscale fluxes and lower negative values of turbulent scale fluxes (Figure S8 in Supporting Information S1). Indicating that the mesoscale fluxes dominate such instances, driving the fraction to be over 1. Similarly for mesoscale fractions <0, the sensible heat flux histograms for scale-resolved fluxes show higher, positive values for turbulent fluxes and lower negative values for mesoscale fluxes causing the mesoscale fraction of the total flux to be negative (Figure S7 in Supporting Information S1). The same phase difference between turbulent and mesoscale fluxes can be seen in the latent heat fluxes too, although they behave more uniformly.

The surface layer friction velocity, u^* can capture the magnitude of surface Reynolds' stress as a velocity scale. For the 1,000 m spatial subintervals, it is calculated from the vertical momentum fluxes as $u^* = \left(\overline{u'w'}^2 + \overline{v'w'}^2\right)^{1/4}$. Similarly, the convective velocity scale $w^* = \left(\frac{g}{\theta_v} z_i \overline{w'\theta_v}\right)^{1/3}$ captures the importance of free convection as a velocity scale. It follows that, u^*/w^* is a non-dimensional parameter that can succinctly capture the competing

Figure 9. H and LE fluxes averaged for flight legs at the same time across all analyzed days for the three Intensive Observation Periods (IOPs). Every day had 2 RFs, a morning and afternoon flight. Every flight had 20 flight legs, numbered 1–20. Each data point is the mean value of fluxes measured from all flight legs at the same time of day in an IOP. The scale-resolved diel time series is shown. *x*-axis shows the mean time of those flight legs in UTC. Since the *x*-axis is ordered according to the flight leg timings, the 2.5 hr break between the end of the morning leg and the start of the afternoon leg is included as discontinuities in the plots. The first column shows the sensible heat flux values (subplots a, c, and e) and the second column shows the latent heat flux values (subplots b, d, and f). Each row shows data for an IOP (a, b July IOP; c, d August IOP; e, f September IOP).

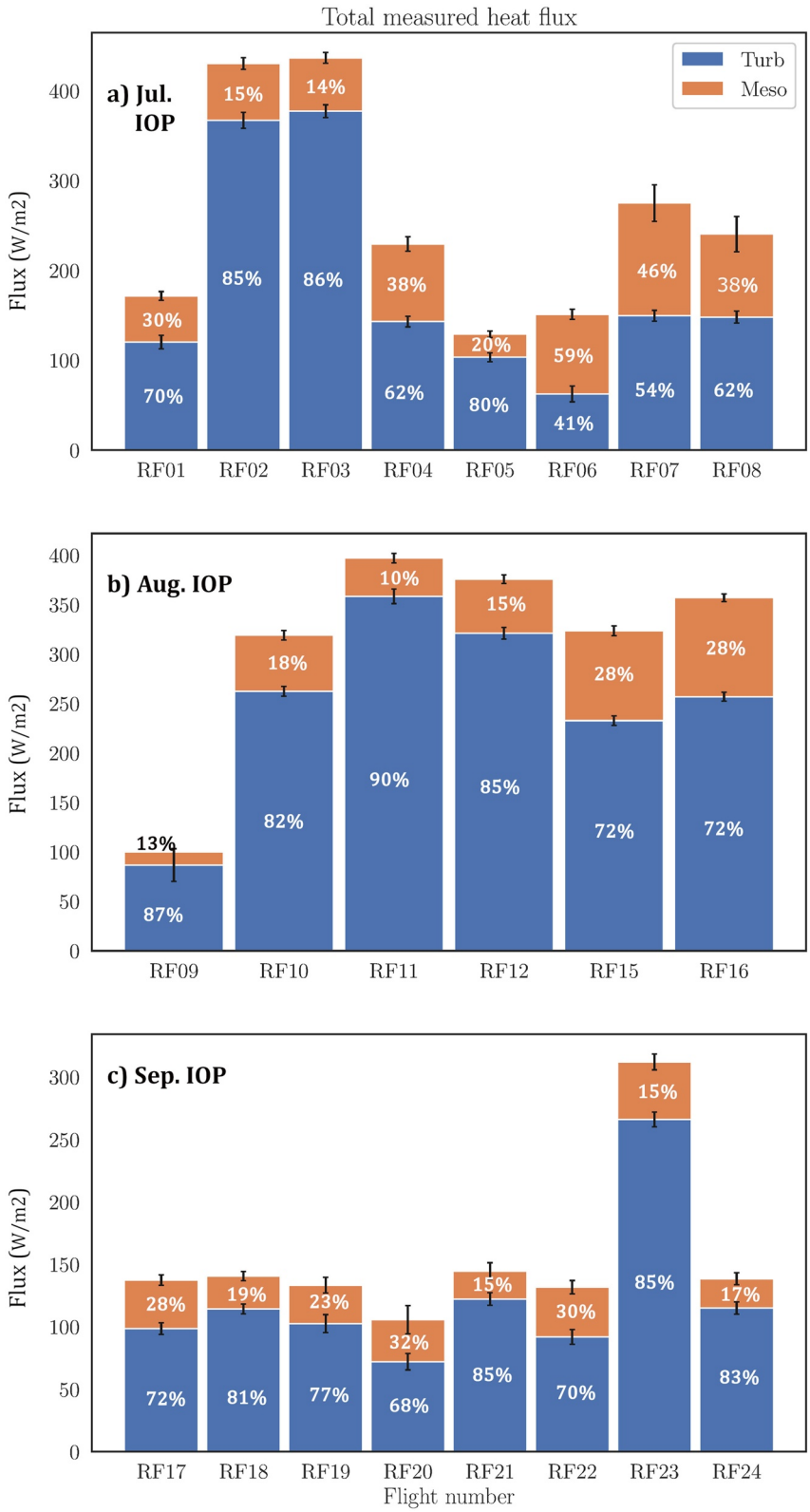

Figure 10. Total (H + LE) fluxes measured on each research flight for all the processed research flight data. The first (a) panel shows flights for the July Intensive Observation Periods (IOPs), the second (b) panel for the August IOP, and the third (c) for the September IOP. Each bar graph represents the mean, scale-resolved flux for a research flight. The *x*-axis shows the research flights and *y*-axis flux magnitudes. Turbulent fluxes in blue and mesoscale fluxes in orange. Percentage contributions in white numbers.

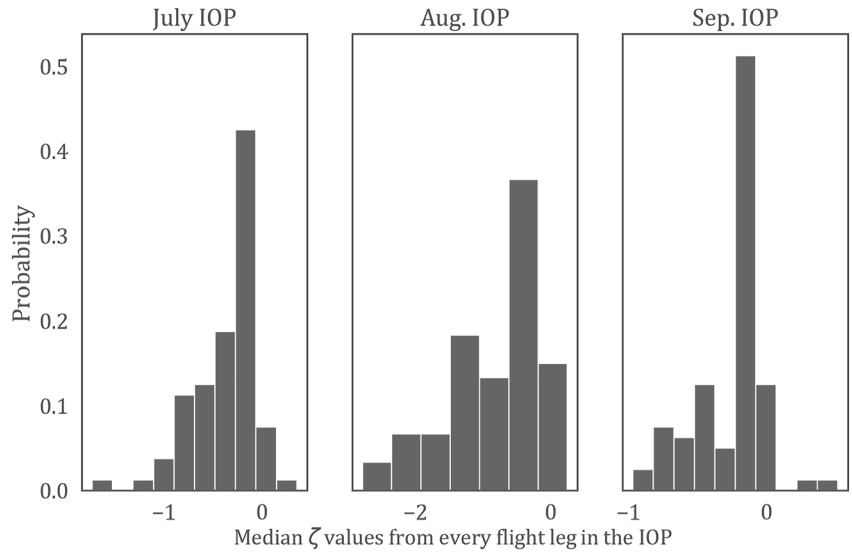

Figure 11. Probability distributions for the atmospheric boundary layer stability parameter, ζ for the three Intensive Observation Periods (IOPs). ζ values were calculated over 1,000 m subintervals along a flight leg. The median values calculated per flight leg are presented here.

effects of free and forced convection in the ABL. If the ABL is strongly shear driven, one would expect higher u^* values and lower w^* values, leading to higher values for u^*/w^* and vice versa for a free convectively driven ABL. Kernel density estimates of u^*/w^* calculated reflect the ζ distribution characteristics for the three IOPs seen earlier in Figure 11. September IOP has a median u^*/w^* value of 0.55, higher than the July (0.45) and August (0.43) IOPs, indicating more shear driven surface atmospheric transport. Similarly, the distributions for July and August IOPs were also similar, with the august IOP having a slightly lower median value indicating more convectively driven transport.

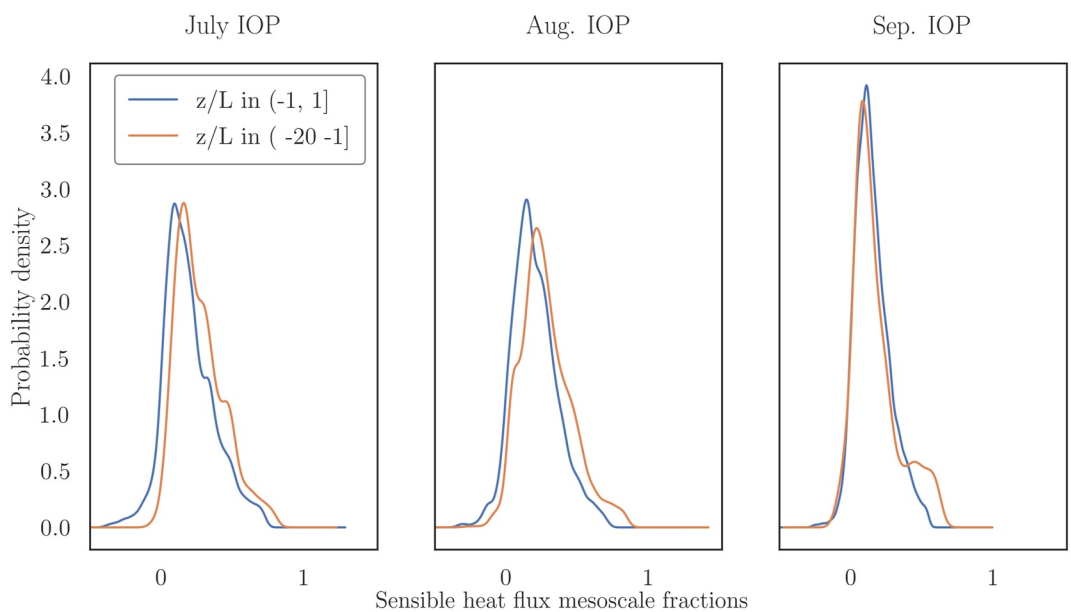

Figure 12. Probability density functions for sensible heat flux mesoscale fractions calculated from kernel density estimates. Mesoscale flux fractions of the total fluxes were calculated over 1,000 m subintervals for the flux space series from every flight leg.

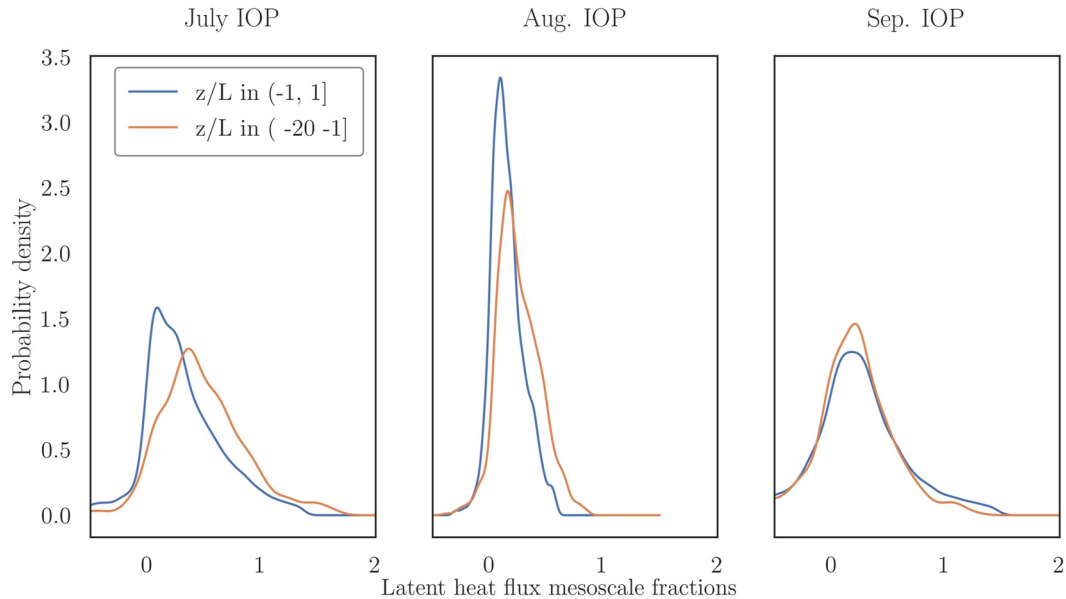

Figure 13. Probability density functions for latent heat flux mesoscale fractions calculated from kernel density estimates. Mesoscale flux fractions of the total fluxes are calculated over 1,000 m subintervals for the flux space series from every flight leg.

A binned scatter plot can help to succinctly visualize non-parametric relationship between two random variables. It has been a popular tool in applied microeconomics to visualize the conditional expectations in large data sets (Chetty et al., 2009; Chetty & Szeidl, 2005; Starr & Goldfarb, 2020). We use the *binsreg* in Python (https://nppackages.github.io/binsreg/) as introduced in Cattaneo et al. (2019). The number of bins for the independent variable of interest is calculated such that it minimizes the integrated mean squared error of the binned scatter (much like a piece wise linear regression). The distribution of the predictor variable is then divided into equal quantiles corresponding to the chosen number of bins and the conditional means of the second variable is calculated.

The mesoscale H percentages show a decreasing trend with increasing u^*/w^* values in July and August IOPs indicating higher mesoscale transport during more convective scenarios (Figure 14a). This is especially clear in the almost flat scatter for the shear driven September IOP data which also has lower magnitudes, with the same order of magnitude throughout the range of u^*/w^* values. The highest values in July and August IOPs are

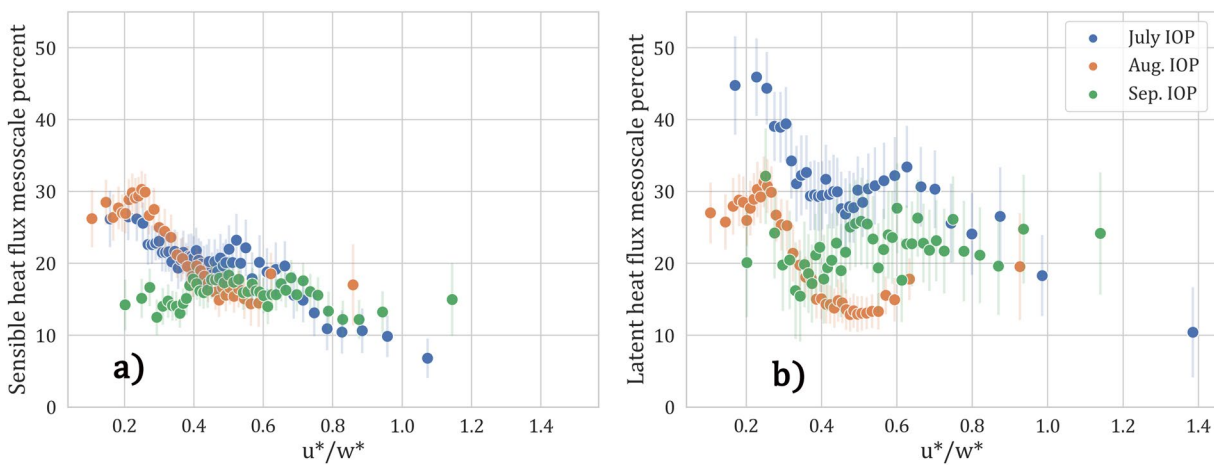

Figure 14. Binned scatter plots of mesoscale flux percentages versus u^*/w^* for all three Intensive Observation Periods (IOPs). Bin values of the flux fractions plotted are calculated as conditional means for the u^*/w^* bins. 95% confidence limits of the mean values are shown as vertical lines at each bin estimate.

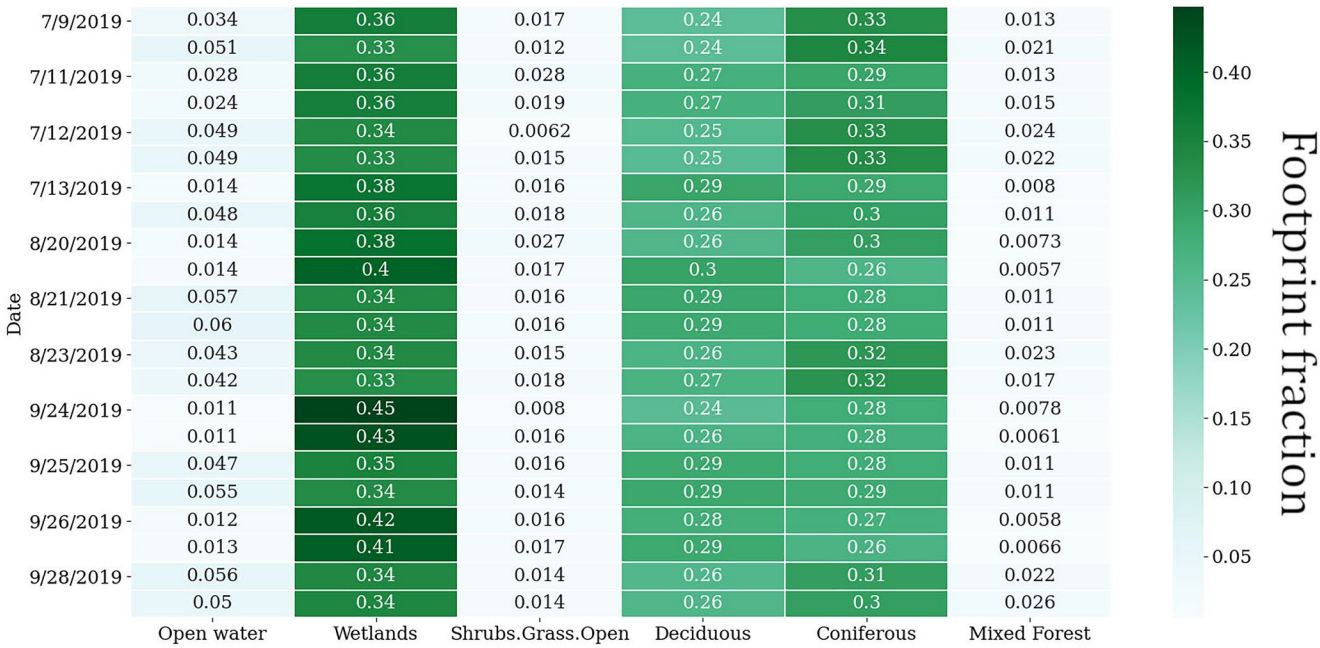

Figure 15. Heat map of fractional footprint contributions from the major land cover classes within the study domain for each research flight. The land cover classes are presented in columns and the airborne campaign dates are presented along rows. The first row for every date corresponds to the morning flight and the second row the afternoon flight. The numbers inside the boxes show fractional footprint contributions and they are colored according to the color bar.

of the same order of magnitude. July IOP shows the lowest percentage values for $u^*/w^* \geq 0.7$. The latent heat mesoscale flux percentages do not behave similarly to the sensible heat flux mesoscale fractions (Figure 14b). Mesoscale fractions measured during the July and August IOPs are higher at lower u^*/w^* values but they are not of the same magnitude. This separation between the magnitudes of the July and August IOP values persists across the range of u^*/w^* values although both the scatters have similar shapes. The August IOP has lower mesoscale LE percentages at lower u^*/w^* values than the July IOP unlike the H mesoscale percentages. The August IOP data also shows the lowest values for mesoscale LE percentages for $u^*/w^* > 0.4$ while July IOP values are consistently the highest across the u^*/w^* range. The same behavior is seen in the IOP averaged mesoscale percentages in Figure 8b where the mesoscale LE percentage for August IOP is the lowest at 18%. Meanwhile, the LE mesoscale percentages during the more shear driven September IOP for $u^*/w^* > 0.4$ show values higher than August IOP. Figure 8b also shows high (29%) mesoscale fluxes for LE in the September IOP. There is also more variation in the September IOP LE values when compared with the H mesoscale percentages for the same time.

3.3.2. Flux Contributions by Land Cover

The land cover class data from Wiscland 2.0 database as shown in Figure 1 for the 40 × 40 km domain was grouped into open water (9% domain area composition), wetlands (34%), deciduous broadleaf forests (30%), shrubs/grass/open land (3.5%), coniferous (22%), and mixed forests (1.3%). Fractional footprint contributions from each of the land cover classes were calculated for each research flight (Figure 15). Wetlands dominate the footprint contributions to the measured fluxes across IOPs as they do for the study domain surface area. They were most prominently sampled during the September IOP research flights of 24 and 26 September, when the UWKA flew a South-East flight pattern with moderate to strong Southerly and South-Westerly winds (Table 1). Further breaking down the wetland class, we find that most of the contributions come from the forested wetlands that account for 27% of the domain area. The deciduous broadleaf forests and coniferous were sampled fairly equally across the IOPs. Although open water bodies showed strong local contributions to the flux space series (for example the blue dots highlighted in the space series shown in Figures 4b and 4c) the averaged contribution during a research flight reflect their lower percentage area composition.

For a more detailed investigation of flux footprint contributions with time, IOP averaged, scale-separated footprint contributions were calculated (Figure 16). For all research flights analyzed, the land cover class with the maximum footprint contribution to the measured fluxes at each 1,000 m subinterval was picked. This was then

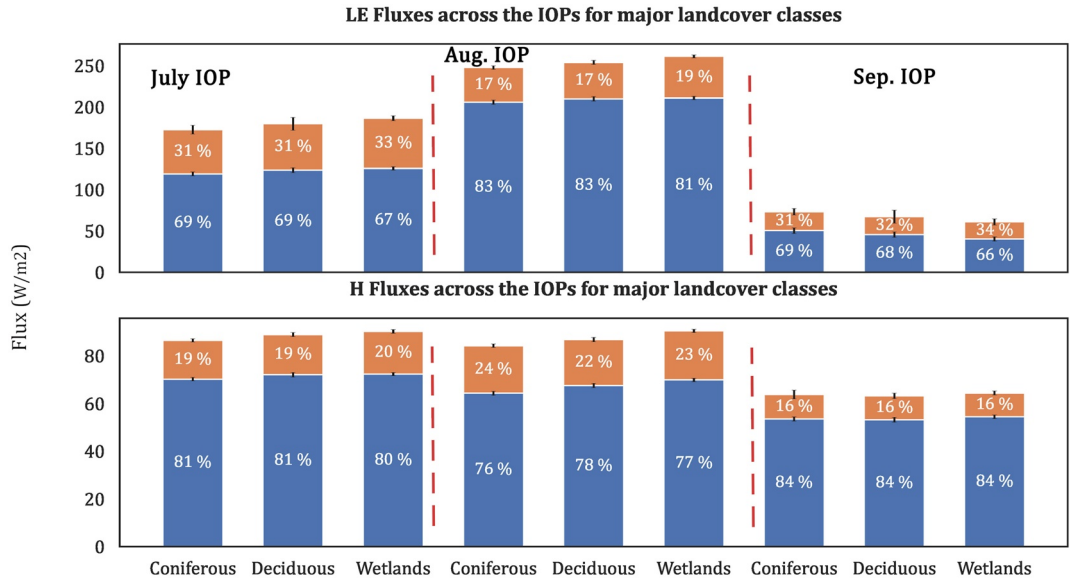

Figure 16. Turbulent and mesoscale sensible and latent heat fluxes measured for the major land cover classes across the Intensive Observation Periods (IOPs). Turbulent fluxes in blue and mesoscale fluxes in orange. Panel on top shows the LE and panel at the bottom shows H. Bar graphs for each of the three IOPs are separated by vertical dashed red lines and ordered as contributions from coniferous, deciduous forests and wetlands within each IOP group.

grouped by their respective IOP to calculate the scale-separated fluxes for each IOP from all the land cover classes. The same overall pattern across the IOPs seen in Figure 8 is repeated in Figure 16 as well, with regards to the magnitudes of the fluxes across IOPs and the scale-resolved percentages. The sensible heat flux magnitudes measured are fairly consistent across the IOPs while the latent heat fluxes show strong seasonality between the IOPs. Although wetlands contribute the most to flux footprints, the scale-composition of the fluxes do not change substantially between the land cover classes. The highest mesoscale LE percentage was measured in the September IOP with all the major land cover classes averaging around 32% and the most H mesoscale percentage values were measured in the July IOP, averaging at 23% between all three land cover classes.

The kernel density estimates for mesoscale fractions did not show significant differences between the three major land cover classes.

3.4. Space Scale Resolved Fluxes

We present a case study for one good flight, with a sample flux topography for a summertime morning flight, RF03, conducted on 11 July 2019 from 09:20 to 11:30 CDT (Central Day Time, 5 hr behind UTC). The flight did east-west transects across the domain, starting from the northern edge and moving to the south. Aircraft logs for the day mention observing shallow cumulus clouds indicating local convection and weak winds for this day. This ensured that the flight transects had a good footprint coverage over the domain for this research flight.

Spatially resolved sensible and latent heat flux topography maps (Figure 17a) show similar order of magnitude values as the IOP averaged behavior in Figure 8. The spatial distribution patterns of both the fluxes do not look similar with latent heat flux showing more spatial variability than the sensible heat flux and dominating over the latter. The percentage mesoscale contributions for the two fluxes are qualitatively similar over the western part of the domain but show differing spatial patterns toward the eastern sections (Figure 17b). These flux topographies illustrate the fact that the CHEESEHEAD19 tower sites inside the study domain sample differing Bowen ratios within the same 10×10 km domain and there are spatially varying, concomitant mesoscale surface-atmospheric transport. This would imply that not all of the towers are sampling the same flux transport and the mesoscale transport associated with their locations would also be different. The flux topographies indicate stronger mesoscale contributions toward the southern edge of the domain in the sensible heat flux plots (Figure 17b). This is due to the inherent time dependency in calculating the topographies from the flight transects. Each research flight duration is about 2 h. This particular flight started measurements at the north end of the domain in early

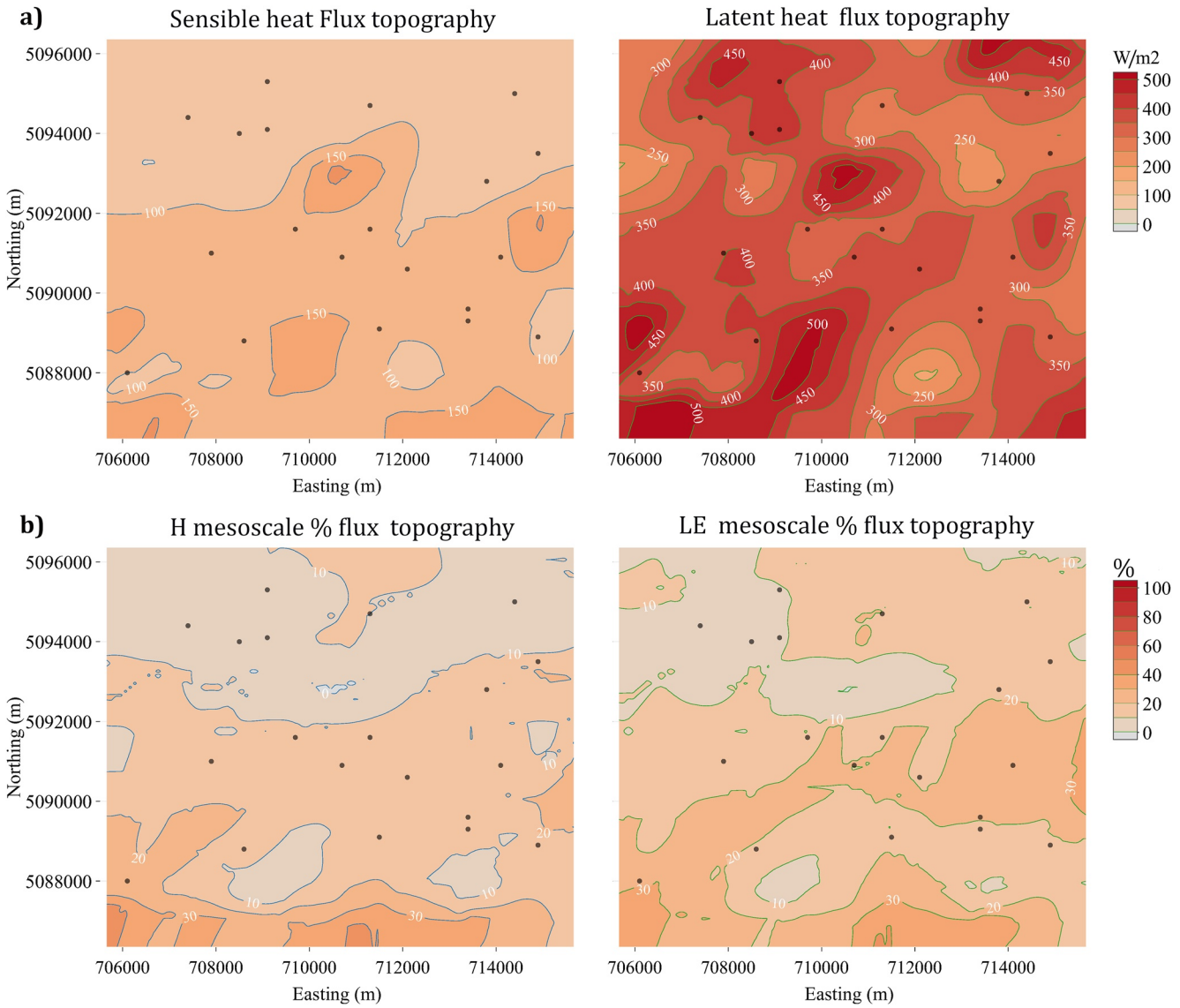

Figure 17. Flux topographies for RF 03 in the July Intensive Observation Period (IOP), 11 July 09:20 to 11:20 CDT over the 10 × 10 km CHEESEHEAD19 core domain. The brown dots are the NCAR-ISFS tower locations. The top row (a) shows the sensible (left) and latent (right) heat flux topographies. The percentage mesoscale contributions to the fluxes are shown in the bottom row (b) below their flux topographies.

morning and by the time it reached the southern edge it was close to noon and by then a fully developed CBL would have formed. Sensible heat mesoscale fluxes develop more later in the day as well (Figures 9a and 9c). The scale-resolved fluxes for latent heat for this flight indicate that the turbulent and meso peaks do not align in space (Figure 18a). Flux topographies for research flights in the August and September IOPs are presented in the supplement along with the standard error percentages for the footprint weighted fluxes (Gatz & Smith, 1995) following Kohnert et al. (2017).

The inherent time dependency of the topographies leads to source strength non-stationarity, since the surface heat flux magnitudes change over the course of the measurement. This makes the flux topographies harder to interpret. A fusion Land Surface Temperature (LST) product over the domain (Desai et al., 2021) for the measurement time shows a high amplitude west-east band in the center (Figure 18b). Mesoscale gradients can be observed close to this band in the latent heat flux plots of Figures 18b and 18c. However, since the large-scale transport would be from quasi-stationary structures we cannot directly link the same to land cover or LST gradients in our current analysis framework.

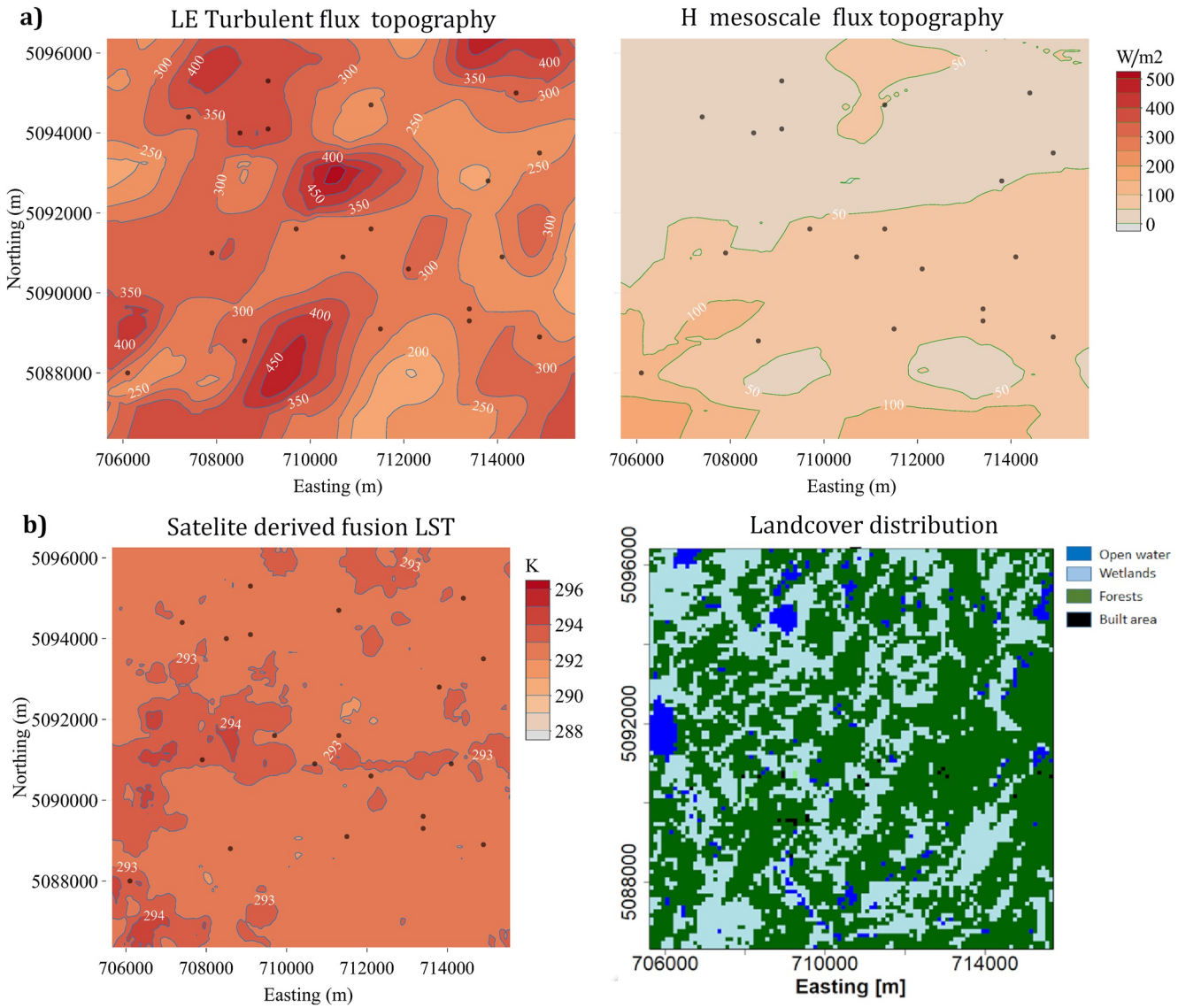

Figure 18. (a) Scale-resolved, turbulent (left) and mesoscale (right) topographies for the latent heat flux and (b) distribution of land-surface properties Land Surface Temperature (LST; left, from Desai et al., 2021) and land-surface classes (right, from Wiscland 2.0) across the domain.

4. Discussion

4.1. Implications for Surface-Atmospheric Transport and Surface Energy Budget Closure

Airborne measurements sampled across the heterogeneous study domain could resolve the constituent surface-atmospheric transport scales. The aircraft campaign experiment design allowed us to measure the diel and seasonal shifts in surface energy balance and investigate its impact on the scales of surface atmospheric transport. We observed higher fractions of mesoscale transport for sensible and latent heat fluxes in convectively driven ABLs as shown in the KDE plots (Figures 12 and 13) in Section 3.3. Previous observational studies have noted the inverse relationship between tower measured surface energy balance imbalance and u^* (Eder et al., 2015; Stoy et al., 2013), indicating that strong mechanical mixing in shear driven ABL leads to larger turbulent transport. Our findings also indicate the same, that lower frequency transport seems to have a preference for convectively driven boundary layers. The dependency of latent heat fluxes is more complicated than the sensible heat flux transport.

Using data from the LITFASS 2003 field experiment in Germany, Foken (2008) and Foken et al. (2010) showed that area averaged surface flux measurements reduce the surface energy budget residuals. This, combined with the observations that the residuals are worse for sites with more heterogeneous surfaces, leads to his hypothesis that what has remained unaccounted for in the budgets could be the transport due to quasi-stationary secondary circulations tied to landscape heterogeneity. The synthesis study by Stoy et al. (2013) found consistent energy balance non-closures across the sites and more importantly, noted that non-closure is linked to the degree of landscape heterogeneity, quantified using MODIS products and GLOBEstat elevation data. Since then a growing body of research has suggested that quasi-stationary low-frequency eddies in the ABL tied to land-surface heterogeneity can play an important role in surface-atmospheric transport.

LES studies with homogeneous (Li & Bou-Zeid, 2011; S. T. Salesky et al., 2017) and heterogeneous (Margairaz et al., 2020, idealized heterogeneities) surface forcings have observed secondary circulations in the ABL transition from convective rolls to a cellular structure as the ABL becomes more convectively unstable. Margairaz et al. (2020) note that for their simulations, with imposed surface temperature heterogeneities in irregular rectangular patches, the convective-cell structure adjusts to the imposed surface temperature variations. The surface atmospheric transport associated with these circulations would be missed by tower based measurements unless they are either swept across the spatially stationary measuring points by the mean wind or only if the point measurements happen to be in their vicinity (Charuchittipan et al., 2014; Mahrt, 2010). These studies along with observations of better closure with longer averaging times and spatial measurements have led to a leading hypothesis that the surface energy balance closure problem is in fact a problem of scale (Foken, 2008; Foken et al., 2010; Mauder et al., 2020).

Large-scale organizations in the form of longitudinal roll vortices, aligned with the mean wind can be generated in daytime CBLs (Etling & Brown, 1993) while stationary circulations can also be induced by horizontal variations in surface roughness and heat flux (Desjardins et al., 1997; Sun et al., 1998). LES studies have shown that over homogeneous surfaces, strongly unstable conditions can lead to the formation of standing convective cells akin to those that form in Rayleigh-Benard convection (De Roo & Mauder, 2018; Kanda et al., 2004). Over heterogeneous surfaces, these free convective cells tend to become quasi-stationary secondary circulations, tied to the surface temperature, roughness, or vegetation gradients (Inagaki et al., 2006; Maronga & Raasch, 2013). Such secondary circulation cells can lead to a persistent local-mean advective transport, leading to an underestimation of surface energy exchange (Morrison et al., 2021).

Desai et al. (2021) present a 50 m resolution fusion LST product for the same study domain, derived using a fusion of land-surface model and satellite products. They note that the spatial standard deviation of the fusion product increases toward autumn and is also high for summer afternoons, with higher LST spatial gradients. This could be playing a role in the higher sensible heat mesoscale fluxes observed in the late morning and afternoon for the July and August IOPs (Figures 9a and 9b).

In this regard, using wavelet methods on high-frequency airborne data has allowed us to retain the larger scale surface-atmosphere transport across the heterogeneous study domain and account for relevant transport scales. Figure 19 shows an IOP averaged representation of the scale resolved fluxes presented in Figures 5–7. We do not see a prominent separation of scales between the turbulent and mesoscale regimes as was reported in the similar study of Mauder, Desjardins, and MacPherson (2007). There is a secondary peak in the LE cospectra for the July IOP around 1,200 m, which persisted across multiple research flights throughout the day (Figures 5a and 5c). Nonetheless, the flux cospectra show consistent and substantial contributions from the mesoscales >2 km. Cospectra calculated for the July and August IOPs show higher values in the larger scales compared to the September IOP cospectrum for both H and LE. The H cospectra for July and August IOPs also show a flattening for scales greater than 5 km. An increase in the magnitude and range of turbulent scales is also seen between the August and September H cospectra. For the LE July and August IOP cospectra, the mesoscale contributions are around the same magnitude. The IOP averaged cospectra for LE also suggest that even with 30 km flight legs we might still be missing contributions from larger scales, with the cospectra tails ending around 150–200 Wm^{-2}.

Looking at the scale-averaged picture, we see that the mesoscale contributions are not a fixed fraction of the total or turbulent fluxes but vary throughout the day and as the landscape undergoes seasonal transitions (Figures 8 and 9). The scale-separated sensible and latent heat fluxes do not behave similarly either. During the August IOP (20–23 August), the measured Bowen ratio is the lowest at 0.3 and this IOP has the lowest mesoscale fraction for latent heat fluxes. Similarly, during the September IOP in early autumn (24–28 September), the Bowen ratio is

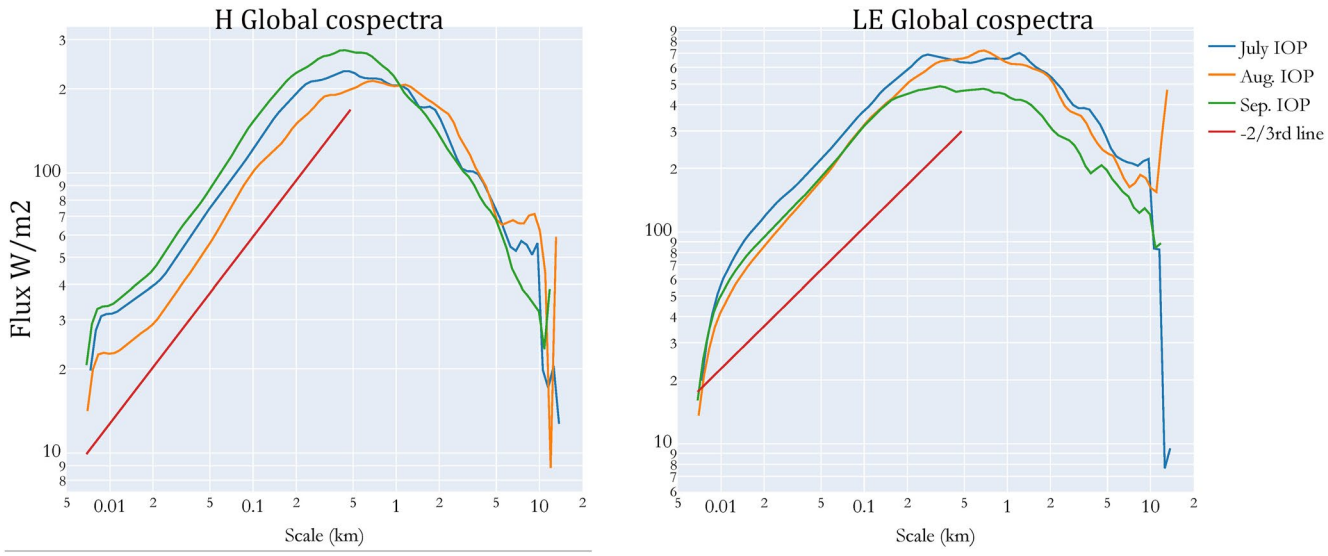

Figure 19. Global cospectra for H and LE for the three Intensive Observation Periods (IOPs). Presented here are the ensemble averages of the wavelet cospectra presented in Figures 5 and 6.

the highest at 1.3 and mesoscale sensible heat flux fraction was the lowest during this IOP. The total mesoscale flux percentages for July IOP = 29%, August IOP = 20%, and September IOP = 21%. The total percentages are closer in magnitude because of the seasonal sensible and latent heat flux balance. It is interesting to note that the August and September IOPs with very different Bowen ratios have the same mesoscale flux percentages.

The scale analysis of surface-atmospheric transport can provide valuable input for process-based parametric correction methods for the tower measured surface energy imbalance. Wanner et al. (2022) present a parametric non-local correction factor for surface energy imbalance extending De Roo et al. (2018) work by incorporating the effects of idealized heterogeneities using data from the LES work by Margairaz et al. (2020). Mauder et al. (2021) (De Roo & Mauder, 2018) method for three midlatitude flux tower sites and found satisfactory results. Currently work is underway to extend the Wanner et al. (2022) method for the CHEESEHEAD19 flux towers and our results on the magnitudes and diel and seasonal variations of mesoscale fluxes can provide valuable order of magnitude benchmarks while correcting for the bias in EC measurements due to the presence of large-scale dispersive fluxes.

We did a comparative study of the aircraft fluxes with flux measurements at 122 m height from the AmeriFlux tall tower at the center of the study domain (US PFa). The tall tower did not have reliable flux data at 122 m height during the August and September IOPs but the comparisons for the July IOP is presented in Figure 20. US PFa makes hourly flux measurements and at 122 m measurement height has a much broader flux footprint than the CHEESEHEAD19 flux towers, with maximum measurement height at 32 m. Here, the wavelet analysis-based airborne fluxes compare reasonably well with the tall tower flux measurements made over a 1 hr averaging window that could include landscape level fluxes.

We tried to extend this approach by comparing total (H + LE) footprint weighted flux measurements from the flux topographies to the total flux measured by the NCAR-ISFS towers in the domain. The flux topographies calculated present a direct and physics-based flux map over the domain for the research flights analyzed, providing a scale-resolved spatial distribution of sensible and latent heat fluxes. They show persistent areas of large-scale flux contributions within the study domain which could be linked to variations of land-surface properties. However, they are also inherently limited by the footprints of airborne transects and can only be extrapolated within those flight transect footprints. Flux measurement in space from the topography was matched with the flux measurement from the tower located in the same 100 × 100 grid point in space and corresponding to the same time as the UWKA data sample. However, for all case studies conducted with six research flights over 3 days in the three IOPs (11 July, 21 August, and 24 September) the scatter plots between fluxes values from the topography grid and the tower measured values did not show any clear relationships. This could be because of

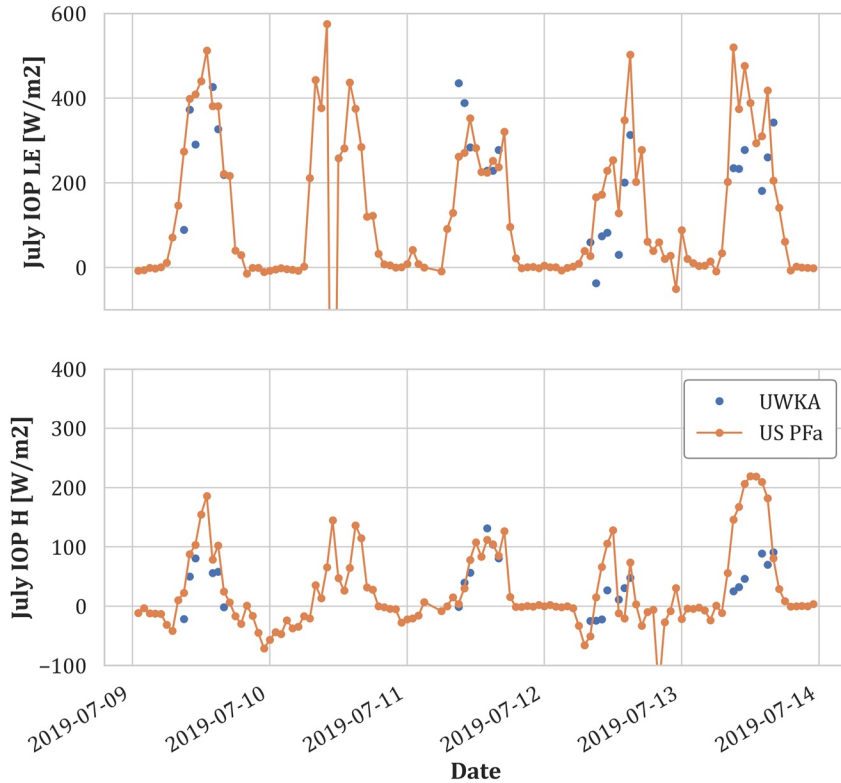

Figure 20. Hourly flux measurements from the University of Wyoming King Air (UWKA) flights and the 122 m tower measurements from the AmeriFlux regional tall tower, US Pfa, at the center of the study domain. Data shown for the July Intensive Observation Period (IOP). The UWKA flux space series was averaged to hourly data points to match the hourly time resolution of the tower measurements.

the vertical flux divergences between the tower measurement heights and the 100 m aircraft measurement height, random errors of tower and flux measurements compounding each other etc.

One should be careful while interpreting footprint-weighted flux maps to study surface-atmospheric transport. The experimental design introduces a temporal element to the topographies calculated in this study. Even though spatially adjacent flight transects during a single flight are only about 6–8 min apart, a research flight across the domain takes about 2.5 hr, imprinting the diel pattern to a calculated flux topography. Kohnert et al. (2017) and Rey-Sanchez et al. (2022) present a flux map based approach to detecting methane hotspots from aircraft and tower measurements, respectively. Unlike methane fluxes, surface heat fluxes have a strong diurnal cycle. Hence, attributing sources for the fluxes solely based on aircraft measured flux topography maps and linking the horizontal flux gradients and surface gradients can be complicated. This presents impactful opportunities to parsimoniously combine aircraft and tower data, when available as is the case for the CHEESEHEAD19 experiment, to arrive at a space-time aligned view of surface fluxes. The airborne campaign numerical experiment design involved calculating space and time resolved flux maps across the domain from simulated tower and aircraft data (from candidate flight patterns) using a machine learning approach with the land-surface properties as drivers (Figure 12 in Metzger et al., 2021).

5. Conclusions

We present a systematic regional-scale observational analysis over a heterogeneous domain that quantifies the multi-scale nature of sub-grid scaling and patterning. The CHEESEHEAD19 field experiment provided a unique data set to diagnose and quantify the diel and seasonal contributions from large-scale transport over the study domain as its surface energy balance shifts from a more latent heat flux-dominated late summer landscape to a more sensible heat flux-dominated early autumn landscape.

Using airborne measurements from this comprehensive field experiment data set, we sought to answer whether spatially resolved airborne eddy covariance can identify spatial scales of surface-atmosphere fluxes over heterogeneous surfaces? Applying wavelet analysis to the airborne flux measurements from the field experiment data allowed us to evaluate and spatially resolve the mesoscale contributions at 100 m above ground over the heterogeneous landscape. The measured heat fluxes were partitioned into turbulent and mesoscale contributions based on a 2,000 m fixed threshold, serving as a proxy for the ABL height, the largest possible length scales for turbulent eddies in the ABL. Although this is supported by the measured observations of ABL heights (Figure 7) and previous studies (Mauder, Desjardins, & MacPherson, 2007; Strunin & Hiyama, 2004), the average flux distribution by scale showed no clear evidence of a particular pattern changing around that scale, especially in the August and September IOPs (Figure 6). We looked at the diel and seasonal variability of the scale-resolved fluxes. The measured latent heat flux magnitudes had more pronounced seasonal changes than the sensible heat fluxes. Meanwhile, the measured domain-averaged sensible heat flux values had a more pronounced diurnal cycle. We observed larger mesoscale transport for sensible heat fluxes in convectively driven ABLs across the three IOP scenarios, while for latent heat fluxes only the July and August IOPs showed more fractional mesoscale transport in convectively driven ABLs. For the September IOP, which had mostly shear driven ABL cases, we did not find any significant change between the fractional mesoscale transport in convectively and shear driven ABLs. We hypothesize that the larger scale transport measured in our study could be linked to organized structures in the ABL as has been reported in previous numerical (Inagaki et al., 2006; Kanda et al., 2004; Margairaz et al., 2020; S. Salesky & Anderson, 2020) and observational (Eder et al., 2015; Morrison et al., 2021) studies. The flux topography case studies indicate that the mesoscale transport spatial variability would be missed by tower measurements in the domain. Areas of persistent contributions in the domain could be linked to the presence of co-located forested wetlands, creating roughness and thermal surface heterogeneities.

From our observations and analyses, we reject our null hypothesis that the mesoscale transport is an invariant, small fixed fraction of total flux. We conclude that our alternate hypothesis, persistent contributions of larger scale (meso-β to meso-γ) fluxes to the daytime sensible and latent heat fluxes exist with diurnal and seasonal variations, holds. We report substantial dissimilarities between the sensible and latent heat flux transport suggesting different physical mechanisms under play, warranting further investigations. The analysis helps further our understanding of the interactions between surface spatial heterogeneity and lower atmosphere feedbacks. Measurements of flux contributions over heterogeneous landscapes have not been studied well. In particular, the shifts associated with seasonal, landscape level transitions as is covered in this study. We believe that this study, by highlighting the importance of larger-scale sub-grid transport, adds a critical piece of information in assimilating and integrating observations and model outputs at multiple scales.

Data Availability Statement

All of the CHEESEHEAD19 observations including UWKA airborne measurements are archived at the NCAR EOL repository at https://www.eol.ucar.edu/field_projects/cheesehead. The eddy4R v.0.2.0 software framework used to generate EC flux estimates can be freely accessed at https://github.com/NEONScience/eddy4R. The eddy4R turbulence v0.0.16 and Environmental Response Functions v0.0.5 software modules for advanced airborne data processing were accessed under Terms of Use for this study (https://www.eol.ucar.edu/content/cheesehead-code-policy-appendix) and are available upon request. The current version of the production code is hosted following a development and systems operation (DevOps) framework for collaborative software development. The DevOps framework allows for a portable, reproducible and extensible EC processing software capabilities that are modular and version controlled using GitHub. The code base is maintained as Docker images to preserve the same dependencies and ensure reproducibility and portability across platforms. Pre-processed input data for the Eddy4R flux processing routines and the calculated scale-resolved fluxes are available at the Ecometeorology lab UW server at http://co2.aos.wisc.edu/data/CHEESEHEAD-incoming/uwka_waveletfluxes/. The python code used to create figures for the manuscript is available at https://github.com/sreenathpaleri/CHEESEHEAD/blob/analysis/scripts/UWKA/manuscript/plot_MS.py.

Acknowledgments
This material is based in part upon work supported by the National Science Foundation through the CHEESEHEAD19 project (Grant AGS-1822420) and the NEON Program (Grant DBI-0752017). The National Ecological Observatory Network is a program sponsored by the National Science Foundation and operated under cooperative agreement by Battelle. Brian Butterworth was additionally supported by the NOAA Physical Sciences Laboratory. Katrin Kohnert and Andrei Serafimovich were supported by the Helmholtz Association of German Research Centres through a Helmholtz Young Investigators Group grant (Grant VH-NG-821) and by the European Union's Horizon 2020 research and innovation program under Grant 72789. We also recognize that our field research occurs on the traditional territories of the Ojibwe people, which have been unjustly ceded and whose ancestors were the original scientists and naturalists who stewarded the land, air, and waters we are fortunate to observe, reflect, and hopefully help continue to flourish.

References

Addison, P. S. (2017). *The illustrated wavelet transform handbook: Introductory theory and applications in science, engineering, medicine, and finance*. CRC press.

Adler, B., Bianco, L., Duncan, J., Turner, D., & Wilczak, J. (2021). NOAA microwave radiometer data and thermodynamic profile retrievals. Version 3.0. UCAR/NCAR—Earth Observing Laboratory ([Dataset] Artwork Size: 6 data files, 2 ancillary/documentation files, 15 GiB Medium: ZIP: PKZIP (application/zip) Pages: 6 data files, 2 ancillary/documentation files, 15 GiB Version Number: 3.0 Type: dataset). Retrieved from https://data.eol.ucar.edu/dataset/592.017

Amiro, B. (1998). Footprint climatologies for evapotranspiration in a boreal catchment. *Agricultural and Forest Meteorology*, *90*(3), 195–201. https://doi.org/10.1016/S0168-1923(97)00096-8

Aubinet, M., Grelle, A., Ibrom, A., Rannik, Ü., Moncrieff, J., Foken, T., et al. (1999). Estimates of the annual net carbon and water exchange of forests: The EUROFLUX methodology. In *Advances in ecological research* (Vol. 30, pp. 113–175). Elsevier. Retrieved from https://linkinghub.elsevier.com/retrieve/pii/S0065250408600185

Aubinet, M., Vesala, T., & Papale, D., (Eds.). (2012). *Eddy covariance: A practical guide to measurement and data analysis*. Springer Netherlands. Retrieved from http://link.springer.com/10.1007/978-94-007-2351-1

Avissar, R., & Schmidt, T. (1998). An evaluation of the scale at which ground-surface heat flux patchiness affects the convective boundary layer using large-eddy simulations. *Journal of the Atmospheric Sciences*, *55*(16), 24–2689. https://doi.org/10.1175/1520-0469(1998)055<2666:aeotsa>2.0.co;2

Baldocchi, D., Falge, E., Gu, L., Olson, R., Hollinger, D., Running, S., et al. (2001). FLUXNET: A new tool to study the temporal and spatial variability of ecosystem-scale carbon dioxide, water vapor, and energy flux densities. *Bulletin of the American Meteorological Society*, *82*(11), 2415–2434. https://doi.org/10.1175/1520-0477(2001)082<2415:FANTTS>2.3.CO;2

Bange, J., Beyrich, F., & Engelbart, D. A. M. (2002). Airborne measurements of turbulent fluxes during LITFASS-98: Comparison with ground measurements and remote sensing in a case study. *Theoretical and Applied Climatology*, *73*(1–2), 35–51. https://doi.org/10.1007/s00704-002-0692-6

Bange, J., Spieß, T., Herold, M., Beyrich, F., & Hennemuth, B. (2006). Turbulent fluxes from Helipod flights above quasi-homogeneous patches within the LITFASS area. *Boundary-Layer Meteorology*, *121*(1), 127–151. https://doi.org/10.1007/s10546-006-9106-0

Berger, B. W., Davis, K. J., Yi, C., Bakwin, P. S., & Zhao, C. L. (2001). Long-term carbon dioxide fluxes from a very tall tower in a northern forest: Flux measurement methodology. *Journal of Atmospheric and Oceanic Technology*, *18*(4), 529–542. https://doi.org/10.1175/1520-0426(2001)018<0529:LTCDFF>2.0.CO;2

Bernhofer, C. (1992). Applying a simple three-dimensional eddy correlation system for latent and sensible heat flux to contrasting forest canopies. *Theoretical and Applied Climatology*, *46*(2–3), 163–172. https://doi.org/10.1007/BF00866096

Bou-Zeid, E., Anderson, W., Katul, G. G., & Mahrt, L. (2020). The persistent challenge of surface heterogeneity in boundary-layer meteorology: A review. *Boundary-Layer Meteorology*, *177*, 227–245. https://doi.org/10.1007/s10546-020-00551-8

Businger, J. A., Wyngaard, J. C., Izumi, Y., & Bradley, E. F. (1971). Flux-profile relationships in the atmospheric surface layer. *Journal of the Atmospheric Sciences*, *28*(2), 181–189. https://doi.org/10.1175/1520-0469(1971)028<0181:FPRITA>2.0.CO;2

Butterworth, B. J., Desai, A. R., Townsend, P. A., Petty, G. W., Andresen, C. G., Bertram, T. H., et al. (2021). Connecting land-atmosphere interactions to surface heterogeneity in CHEESEHEAD19. *Bulletin of the American Meteorological Society*, *102*(2), E421–E445. https://doi.org/10.1175/BAMS-D-19-0346.1

Cattaneo, M. D., Crump, R. K., Farrell, M. H., & Feng, Y. (2019). Binscatter regressions. arXiv preprint arXiv:1902.09615. [Software]. https://doi.org/10.48550/arXiv.1902.09608

Charuchittipan, D., Babel, W., Mauder, M., Leps, J.-P., & Foken, T. (2014). Extension of the averaging time in eddy-covariance measurements and its effect on the energy balance closure. *Boundary-Layer Meteorology*, *152*(3), 303–327. https://doi.org/10.1007/s10546-014-9922-6

Chetty, R., Looney, A., & Kroft, K. (2009). Salience and taxation: Theory and evidence. *The American Economic Review*, *99*(4), 1145–1177. https://doi.org/10.1257/aer.99.4.1145

Chetty, R., & Szeidl, A. (2005). *Marriage, housing, and portfolio choice: A test of Grossman-Laroque*. Mimeograph.

Davis, K. J., Bakwin, P. S., Yi, C., Berger, B. W., Zhao, C., Teclaw, R. M., & Isebrands, J. G. (2003). The annual cycles of CO_2 and H_2O exchange over a northern mixed forest as observed from a very tall tower. *Global Change Biology*, *9*(9), 1278–1293. https://doi.org/10.1046/j.1365-2486.2003.00672.x

De Roo, F., & Mauder, M. (2018). The influence of idealized surface heterogeneity on virtual turbulent flux measurements. *Atmospheric Chemistry and Physics*, *18*(7), 5059–5074. https://doi.org/10.5194/acp-18-5059-2018

De Roo, F., Zhang, S., Huq, S., & Mauder, M. (2018). A semi-empirical model of the energy balance closure in the surface layer. *PLoS One*, *13*(12), e0209022. https://doi.org/10.1371/journal.pone.0209022

Desai, A. R. (2014). Influence and predictive capacity of climate anomalies on daily to decadal extremes in canopy photosynthesis. *Photosynthesis Research*, *119*(1–2), 31–47. https://doi.org/10.1007/s11120-013-9925-z

Desai, A. R., Khan, A. M., Zheng, T., Paleri, S., Butterworth, B., Lee, T. R., et al. (2021). Multi-sensor approach for high space and time resolution land surface temperature. *Earth and Space Science*, *8*(10). https://doi.org/10.1029/2021EA001842

Desai, A. R., Xu, K., Tian, H., Weishampel, P., Thom, J., Baumann, D., et al. (2015). Landscape-level terrestrial methane flux observed from a very tall tower. *Agricultural and Forest Meteorology*, *201*, 61–75. https://doi.org/10.1016/j.agrformet.2014.10.017

Desjardins, R. L., MacPherson, J. I., Mahrt, L., Schuepp, P., Pattey, E., Neumann, H., et al. (1997). Scaling up flux measurements for the boreal forest using aircraft-tower combinations. *Journal of Geophysical Research: Atmospheres*, *102*(D24), 29125–29133. https://doi.org/10.1029/97JD00278

Drobinski, P., Brown, R. A., Flamant, P. H., & Pelon, J. (1998). Evidence of organized large eddies by ground-based Doppler Lidar, sonic anemometer and sodar. *Boundary-Layer Meteorology*, *88*(3), 343–361. https://doi.org/10.1023/A:1001167212584

Duncan, J. B., Jr., Bianco, L., Adler, B., Bell, T., Djalalova, I. V., Riihimaki, L., et al. (2022). Evaluating convective planetary boundary layer height estimations resolved by both active and passive remote sensing instruments during the CHEESEHEAD19 field campaign. *Atmospheric Measurement Techniques*, *15*(8), 2479–2502. https://doi.org/10.5194/amt-15-2479-2022

Eder, F., Schmidt, M., Damian, T., Träumner, K., & Mauder, M. (2015). Mesoscale eddies affect near-surface turbulent exchange: Evidence from Lidar and tower measurements. *Journal of Applied Meteorology and Climatology*, *54*(1), 189–206. https://doi.org/10.1175/JAMC-D-14-0140.1

Engelmann, C., & Bernhofer, C. (2016). Exploring eddy-covariance measurements using a spatial approach: The eddy matrix. *Boundary-Layer Meteorology*, *161*(1), 1–17. https://doi.org/10.1007/s10546-016-0161-x

Etling, D., & Brown, R. A. (1993). Roll vortices in the planetary boundary layer: A review. *Boundary-Layer Meteorology*, *65*(3), 215–248. https://doi.org/10.1007/BF00705527

Farge, M. (1992). Wavelet transforms and their applications to turbulence (p. 64).
Finnigan, J. J., Clement, R., Malhi, Y., Leuning, R., & Cleugh, H. (2003). A Re-evaluation of long-term flux measurement techniques Part I: Averaging and coordinate rotation. *Boundary-Layer Meteorology*, *107*(1), 1–48. https://doi.org/10.1023/A:1021554900225
Foken, T. (2008). The energy balance closure problem: An overview. *Ecological Applications*, *18*(6), 1351–1367. https://doi.org/10.1890/06-0922.1
Foken, T. (2017). *Micrometeorology*. Springer Berlin Heidelberg. Retrieved from http://link.springer.com/10.1007/978-3-642-25440-6
Foken, T., Mauder, M., Liebethal, C., Wimmer, F., Beyrich, F., Leps, J.-P., et al. (2010). Energy balance closure for the LITFASS-2003 experiment. *Theoretical and Applied Climatology*, *101*(1–2), 149–160. https://doi.org/10.1007/s00704-009-0216-8
Foken, T., Wimmer, F., Mauder, M., Thomas, C., & Liebethal, C. (2006). Some aspects of the energy balance closure problem. *Atmospheric Chemistry and Physics*, *8*(12), 4395–4402. https://doi.org/10.5194/acp-6-4395-2006
French, J., Oolman, L., & Plummer, D. (2021). University of Wyoming King Air (UWKA) high rate flight level data. Version 1.0. UCAR/NCAR—Earth Observing Laboratory ([Dataset] Artwork Size: 24 data files, 2 ancillary/documentation files, 3 GiB Medium: NetCDF: Network Common Data Form (application/x-netcdf) Pages: 24 data files, 2 ancillary/documentation files, 3 GiB Version Number: 1.0 Type: dataset). Retrieved from https://data.eol.ucar.edu/dataset/592.146
Gao, Z., Liu, H., Chen, X., Huang, M., Missik, J. E. C., Yao, J., et al. (2020). Enlarged nonclosure of surface energy balance with increasing atmospheric instabilities linked to changes in coherent structures. *Journal of Geophysical Research: Atmospheres*, *125*(14). https://doi.org/10.1029/2020JD032889
Gatz, D. F., & Smith, L. (1995). The standard error of a weighted mean concentration—I. Bootstrapping vs other methods. *Atmospheric Environment*, *29*(11), 1185–1193. https://doi.org/10.1016/1352-2310(94)00210-C
Haimov, S., & Rodi, A. (2013). Fixed-antenna pointing-angle calibration of airborne Doppler cloud radar. *Journal of Atmospheric and Oceanic Technology*, *30*(10), 2320–2335. https://doi.org/10.1175/JTECH-D-12-00262.1
Hartmann, J., Gehrmann, M., Kohnert, K., Metzger, S., & Sachs, T. (2018). New calibration procedures for airborne turbulence measurements and accuracy of the methane fluxes during the AirMeth campaigns. *Atmospheric Measurement Techniques*, *11*(7), 4567–4581. https://doi.org/10.5194/amt-11-4567-2018
Higgins, C. W., Pardyjak, E., Froidevaux, M., Simeonov, V., & Parlange, M. B. (2013). Measured and estimated water vapor advection in the atmospheric surface layer. *Journal of Hydrometeorology*, *14*(6), 1966–1972. https://doi.org/10.1175/JHM-D-12-0166.1
Högström, U. (1988). Non-dimensional wind and temperature profiles in the atmospheric surface layer: A re-evaluation. *Boundary-Layer Meteorology*, *42*(1), 55–78. https://doi.org/10.1007/BF00119875
Iglewicz, B., & Hoaglin, D. C. (1993). *How to detect and handle outliers* (Vol. 16). Asq Press.
Inagaki, A., Letzel, M. O., Raasch, S., & Kanda, M. (2006). Impact of surface heterogeneity on energy imbalance: A study using LES. *Journal of the Meteorological Society of Japan*, *84*(1), 187–198. https://doi.org/10.2151/jmsj.84.187
Kaimal, J. C., & Finnigan, J. J. (1994). *Atmospheric boundary layer flows: Their structure and measurement*. Oxford University Press.
Kanda, M., Inagaki, A., Letzel, M. O., Raasch, S., & Watanabe, T. (2004). LES study of the energy imbalance problem with eddy covariance fluxes. *Boundary-Layer Meteorology*, *110*(3), 381–404. https://doi.org/10.1023/B:BOUN.0000007225.45548.7a
Kljun, N., Calanca, P., Rotach, M. W., & Schmid, H. P. (2004). A simple parameterization for flux footprint predictions. *Boundary-Layer Meteorology*, *112*(3), 503–523. https://doi.org/10.1023/B:BOUN.0000030653.71031.96
Kljun, N., Rotach, M., & Schmid, H. (2002). A three-dimensional backward Lagrangian footprint model for A wide range of boundary-layer stratifications. *Boundary-Layer Meteorology*, *103*(2), 205–226. https://doi.org/10.1023/A:1014556300021
Kohnert, K., Serafimovich, A., Metzger, S., Hartmann, J., & Sachs, T. (2017). Strong geologic methane emissions from discontinuous terrestrial permafrost in the Mackenzie Delta, Canada. *Scientific Reports*, *7*(1), 5828. https://doi.org/10.1038/s41598-017-05783-2
Lenschow, D. H., Mann, J., & Kristensen, L. (1994). How long is long enough when measuring fluxes and other turbulence statistics? *Journal of Atmospheric and Oceanic Technology*, *11*(3), 661–673. https://doi.org/10.1175/1520-0426(1994)011<0661:HLILEW>2.0.CO;2
Lenschow, D. H., & Stankov, B. B. (1986). Length scales in the convective boundary layer. *Journal of the Atmospheric Sciences*, *43*(12), 1198–1209. https://doi.org/10.1175/1520-0469(1986)043<1198:LSITCB>2.0.CO;2
Li, D., & Bou-Zeid, E. (2011). Coherent structures and the dissimilarity of turbulent transport of momentum and scalars in the unstable atmospheric surface layer. *Boundary-Layer Meteorology*, *140*(2), 243–262. https://doi.org/10.1007/s10546-011-9613-5
Mahrt, L. (1998). Flux sampling errors for aircraft and towers. *Journal of Atmospheric and Oceanic Technology*, *15*(2), 14–429. https://doi.org/10.1175/1520-0426(1998)015<0416:fsefaa>2.0.co;2
Mahrt, L. (2010). Computing turbulent fluxes near the surface: Needed improvements. *Agricultural and Forest Meteorology*, *150*(4), 501–509. https://doi.org/10.1016/j.agrformet.2010.01.015
Margairaz, F., Pardyjak, E. R., & Calaf, M. (2020). Surface thermal heterogeneities and the atmospheric boundary layer: The relevance of dispersive fluxes. *Boundary-Layer Meteorology*, *175*(3), 369–395. https://doi.org/10.1007/s10546-020-00509-w
Maronga, B., & Raasch, S. (2013). Large-eddy simulations of surface heterogeneity effects on the convective boundary layer during the LITFASS-2003 experiment. *Boundary-Layer Meteorology*, *146*(1), 17–44. https://doi.org/10.1007/s10546-012-9748-z
Mauder, M., Desjardins, R. L., & MacPherson, I. (2007). Scale analysis of airborne flux measurements over heterogeneous terrain in a boreal ecosystem: Scale analysis of flux measurements. *Journal of Geophysical Research: Atmospheres*, *112*(D13), 2006JD008133. https://doi.org/10.1029/2006JD008133
Mauder, M., Desjardins, R. L., & MacPherson, I. (2008). Creating surface flux maps from airborne measurements: Application to the Mackenzie Area GEWEX Study MAGS 1999. *Boundary-Layer Meteorology*, *129*(3), 431–450. https://doi.org/10.1007/s10546-008-9326-6
Mauder, M., Desjardins, R. L., Pattey, E., Gao, Z., & van Haarlem, R. (2008). Measurement of the sensible eddy heat flux based on spatial averaging of continuous ground-based observations. *Boundary-Layer Meteorology*, *128*(1), 151–172. https://doi.org/10.1007/s10546-008-9279-9
Mauder, M., Foken, T., & Cuxart, J. (2020). Surface-energy-balance closure over land: A review. *Boundary-layer meteorology*, *177*, 395–426. https://doi.org/10.1007/s10546-020-00529-6
Mauder, M., Ibrom, A., Wanner, L., De Roo, F., Brugger, P., Kiese, R., & Pilegaard, K. (2021). Options to correct local turbulent flux measurements for large-scale fluxes using a LES-based approach (preprint). Others (Wind, Precipitation, Temperature, etc.)/In Situ Measurement/Data Processing and Information Retrieval. Retrieved from https://amt.copernicus.org/preprints/amt-2021-126/
Mauder, M., Oncley, S. P., Vogt, R., Weidinger, T., Ribeiro, L., Bernhofer, C., et al. (2007). The Energy Balance Experiment EBEX-2000. Part II: Intercomparison of eddy-covariance sensors and post-field data processing methods. *Boundary-Layer Meteorology*, *123*(1), 29–54. https://doi.org/10.1007/s10546-006-9139-4
Meijninger, W. M. L., Beyrich, F., Lüdi, A., Kohsiek, W., & Bruin, H. A. R. D. (2006). Scintillometer-based turbulent fluxes of sensible and latent heat over a heterogeneous land surface—A contribution to Litfass-2003. *Boundary-Layer Meteorology*, *121*(1), 89–110. https://doi.org/10.1007/s10546-005-9022-8

Metzger, S., Durden, D., Paleri, S., Sühring, M., Butterworth, B. J., Florian, C., et al. (2021). Novel approach to observing system simulation experiments improves information gain of surface-atmosphere field measurements. *Atmospheric Measurement Techniques*, *14*(11), 6929–6954. https://doi.org/10.5194/amt-14-6929-2021

Metzger, S., Durden, D., Sturtevant, C., Luo, H., Pingintha-Durden, N., Sachs, T., et al. (2017). eddy4R 0.2.0: A DevOps model for community-extensible processing and analysis of eddy-covariance data based on R, Git, Docker, and HDF5. *Geoscientific Model Development*, *10*(9), 3189–3206. https://doi.org/10.5194/gmd-10-3189-2017

Metzger, S., Junkermann, W., Mauder, M., Butterbach-Bahl, K., Trancón y Widemann, B., Neidl, F., et al. (2013). Spatially explicit regionalization of airborne flux measurements using environmental response functions. *Biogeosciences*, *10*(4), 2193–2217. https://doi.org/10.5194/bg-10-2193-2013

Monin, A., & Obukhov, A. (1954). Osnovnye zakonomernosti turbulentnogo peremeshivanija v prizemnom sloe atmosfery (basic laws of turbulent mixing in the atmosphere near the ground). *Trudy Geofiz. Instituta Akademiya Nauk SSSR*, *24*(151), 163–187.

Morrison, T., Calaf, M., Higgins, C. W., Drake, S. A., Perelet, A., & Pardyjak, E. (2021). The impact of surface temperature heterogeneity on near-surface heat transport. *Boundary-Layer Meteorology*, *180*(2), 247–272. https://doi.org/10.1007/s10546-021-00624-2

Nordbo, A., & Katul, G. (2013). A wavelet-based correction method for eddy-covariance high-frequency losses in scalar concentration measurements. *Boundary-Layer Meteorology*, *146*(1), 81–102. https://doi.org/10.1007/s10546-012-9759-9

Obukhov, A. (1946). Turbulentnost'v temperaturnoj-neodnorodnoj atmosfere. *Trudy Instituta Teoreticheskoi Geofiziki, Akademiya Nauk SSSR*, *1*, 95–115.

Oncley, S. P., Foken, T., Vogt, R., Kohsiek, W., DeBruin, H. A. R., Bernhofer, C., et al. (2007). The Energy Balance Experiment EBEX-2000. Part I: Overview and energy balance. *Boundary-Layer Meteorology*, *123*(1), 1–28. https://doi.org/10.1007/s10546-007-9161-1

Orlanski, I. (1975). A rational subdivision of scales for atmospheric processes. *Bulletin of the American Meteorological Society*, 527–530.

Pielke, R. A., Sr., Avissar, R., Raupach, M., Dolman, A. J., Zeng, X., & Denning, A. S. (1998). Interactions between the atmosphere and terrestrial ecosystems: Influence on weather and climate. *Global Change Biology*, *4*(5), 461–475. https://doi.org/10.1046/j.1365-2486.1998.t01-1-00176.x

Rey-Sanchez, C., Arias-Ortiz, A., Kasak, K., Chu, H., Szutu, D., Verfaillie, J., & Baldocchi, D. (2022). Detecting hot spots of methane flux using footprint-weighted flux maps. *Journal of Geophysical Research: Biogeosciences*, *127*(8), e2022JG006977. https://doi.org/10.1029/2022jg006977

Rodi, A. (2011). King of the air: The evolution and capabilities of Wyoming's observation aircraft. *Meteorological Technology International*, 44–47.

Rodi, A. R., & Leon, D. C. (2012). Correction of static pressure on a research aircraft in accelerated flight using differential pressure measurements. *Atmospheric Measurement Techniques*, *5*(11), 2569–2579. https://doi.org/10.5194/amt-5-2569-2012

Rodi, A. R., & Spyers-Duran, P. A. (1972). Analysis of time response of airborne temperature sensors. *Journal of Applied Meteorology and Climatology*, *11*(3), 554–556. https://doi.org/10.1175/1520-0450(1972)011<0554:AOTROA>2.0.CO;2

Salesky, S., & Anderson, W. (2020). Coherent structures modulate atmospheric surface layer flux-gradient relationships. *Physical Review Letters*, *125*(12), 124501. https://doi.org/10.1103/PhysRevLett.125.124501

Salesky, S. T., Chamecki, M., & Bou-Zeid, E. (2017). On the nature of the transition between roll and cellular organization in the convective boundary layer. *Boundary-Layer Meteorology*, *163*(1), 41–68. https://doi.org/10.1007/s10546-016-0220-3

Scott, D. W. (1979). On optimal and data-based histograms. *Biometrika*, *66*(3), 605–610. https://doi.org/10.1093/biomet/66.3.605

Scott, D. W. (2015). *Multivariate density estimation: Theory, practice, and visualization*. John Wiley & Sons.

Starr, E., & Goldfarb, B. (2020). Binned scatterplots: A simple tool to make research easier and better. *Strategic Management Journal*, *41*(12), 2261–2274. https://doi.org/10.1002/smj.3199

Steinfeld, G., Letzel, M. O., Raasch, S., Kanda, M., & Inagaki, A. (2007). Spatial representativeness of single tower measurements and the imbalance problem with eddy-covariance fluxes: Results of a large-eddy simulation study. *Boundary-Layer Meteorology*, *123*(1), 77–98. https://doi.org/10.1007/s10546-006-9133-x

Stoy, P. C., Mauder, M., Foken, T., Marcolla, B., Boegh, E., Ibrom, A., et al. (2013). A data-driven analysis of energy balance closure across FLUXNET research sites: The role of landscape scale heterogeneity. *Agricultural and Forest Meteorology*, *171–172*, 137–152. https://doi.org/10.1016/j.agrformet.2012.11.004

Strunin, M. A., & Hiyama, T. (2004). Applying wavelet transforms to analyze aircraft measured turbulence and turbulent fluxes in the atmospheric boundary layer over eastern Siberia. *Hydrological Processes*, *18*(16), 3081–3098. https://doi.org/10.1002/hyp.5750

Strunin, M. A., & Hiyama, T. (2005). Spectral structure of small-scale turbulent and mesoscale fluxes in the atmospheric boundary layer over a thermally inhomogeneous land surface. *Boundary-Layer Meteorology*, *117*(3), 479–510. https://doi.org/10.1007/s10546-005-2188-2

Strunin, M. A., Hiyama, T., Asanuma, J., & Ohata, T. (2004). Aircraft observations of the development of thermal internal boundary layers and scaling of the convective boundary layer over non-homogeneous land surfaces. *Boundary-Layer Meteorology*, *111*(3), 491–522. https://doi.org/10.1023/B:BOUN.0000016542.72958.e9

Stull, R. B. (1988). An introduction to boundary layer meteorology. In R. B. Stull (Ed.), *An introduction to boundary layer meteorology* (pp. 1–27). : Springer Netherlands. Retrieved from http://link.springer.com/10.1007/978-94-009-3027-8_1

Sun, J., Desjardins, R., Mahrt, L., & MacPherson, I. (1998). Transport of carbon dioxide, water vapor, and ozone by turbulence and local circulations. *Journal of Geophysical Research: Atmospheres*, *103*(D20), 25873–25885. https://doi.org/10.1029/98JD02439

Thomas, C., & Foken, T. (2005). Detection of long-term coherent exchange over spruce forest using wavelet analysis. *Theoretical and Applied Climatology*, *80*(2–4), 91–104. https://doi.org/10.1007/s00704-004-0093-0

Torrence, C., & Compo, G. P. (1998). A practical guide to wavelet analysis. *Bulletin of the American Meteorological Society*, *79*(1), 18–78. https://doi.org/10.1175/1520-0477(1998)079<0061:apgtwa>2.0.co;2

Wang, Z., French, J., Vali, G., Wechsler, P., Haimov, S., Rodi, A., et al. (2012). Single aircraft integration of remote sensing and in situ sampling for the study of cloud microphysics and dynamics. *Bulletin of the American Meteorological Society*, *93*(5), 653–668. https://doi.org/10.1175/BAMS-D-11-00044.1

Wanner, L., Calaf, M., & Mauder, M. (2022). Incorporating the effect of heterogeneous surface heating into a semi-empirical model of the surface energy balance closure. *PLoS One*, *17*(6), e0268097. https://doi.org/10.1371/journal.pone.0268097

Wulfmeyer, V., Turner, D. D., Baker, B., Banta, R., Behrendt, A., Bonin, T., et al. (2018). A new research approach for observing and characterizing land-atmosphere feedback. *Bulletin of the American Meteorological Society*, *99*(8), 1639–1667. https://doi.org/10.1175/BAMS-D-17-0009.1

Xu, F., Wang, W., Wang, J., Xu, Z., Qi, Y., & Wu, Y. (2017). Area-averaged evapotranspiration over a heterogeneous land surface: Aggregation of multi-point EC flux measurements with a high-resolution land-cover map and footprint analysis. *Hydrology and Earth System Sciences*, *21*(8), 4037–4051. https://doi.org/10.5194/hess-21-4037-2017

Xu, K., Sühring, M., Metzger, S., Durden, D., & Desai, A. R. (2020). Can data mining help eddy covariance see the landscape? A large-eddy simulation study. *Boundary-Layer Meteorology*, *176*, 85–103. https://doi.org/10.1007/s10546-020-00513-0

Zhang, G., Leclerc, M. Y., Duarte, H. F., Durden, D., Werth, D., Kurzeja, R., & Parker, M. (2014). Multi-scale decomposition of turbulent fluxes above a forest canopy. *Agricultural and Forest Meteorology*, *186*, 48–63. https://doi.org/10.1016/j.agrformet.2013.11.010

Zhang, Y., Liu, H., Foken, T., Williams, Q. L., Liu, S., Mauder, M., & Liebethal, C. (2010). Turbulence spectra and cospectra under the influence of large eddies in the Energy Balance EXperiment (EBEX). *Boundary-Layer Meteorology*, *136*(2), 235–251. https://doi.org/10.1007/s10546-010-9504-1

Zhou, Y., Li, D., & Li, X. (2019). The effects of surface heterogeneity scale on the flux imbalance under free convection. *Journal of Geophysical Research: Atmospheres*, *124*, 8424–8448. https://doi.org/10.1029/2018JD029550